Self-Sorting of Deformable Particles in a Microfluidic Circuit

by

Mohamed Salem Raafat

B. Eng. Mechanical Design and Production,
Faculty of Engineering, Cairo University, 2003

Submitted to the Department of Mechanical Engineering
in partial fulfillment of the requirements for the degree of

Master of Science in Mechanical Engineering

at the

MASSACHUSETTS INSTITUTE OF TECHNOLOGY

September 2010

Signature of Author . . . . . .

Department of Mechanical Engineering
August 20, 2010

Certified by . . . . . .

Rohit N. Karnik
d'Arbeloff Assistant Professor of Mechanical Engineering
Thesis Supervisor

Accepted by . . . . . .

David E. Hardt
Professor of Mechanical Engineering
Graduate Officer

(This page is intentionally left blank)

Self-Sorting of Deformable Particles in a Microfluidic Circuit

by

Mohamed Salem Raafat

Submitted to the Department of Mechanical Engineering on August 20, 2010,
in partial fulfillment of the requirements for the degree of
Master of Science in Mechanical Engineering

Abstract

In this thesis, a new microfluidic device is presented for sorting of deformable particles based on the hydrodynamic resistance induced in a microchannel. Hydrodynamic resistance can be related to physical properties, including size and deformability of the particle, and can also be influenced by particle-wall interactions, hence allowing sorting based on any of these characteristics. This device could find application in cell sorting and bioseparation for therapeutics, research, and point-of-care diagnostics, as well as in sorting of droplets and emulsions for research and industrial applications (e.g., pharmaceutics, food industry, etc.). The device design is carried out using an equivalent resistance model, and numerical simulations are used to validate the design. The device is fabricated in PDMS, flow velocities are characterized using particle streak velocimetry, and sorting experiments are conducted to sort deformable gelatin particles according to size, and droplets of water and glycerol according to deformability. A sorting resolution of approximately 1 μm was obtained when sorting based on size, and droplets of water and glycerol were sorted into separate streams when sorting based on deformability. The main strength of the device over existing technology lies in its simplicity: sorting is carried out passively in the microfluidic circuit, eliminating the need for additional detection or sorting modules. Moreover, the device could be easily customized to change the sorting parameter or the sorting threshold, and multiple devices can be combined in parallel (to increase throughput) or in series (to increase resolution).

Thesis supervisor: Rohit N. Karnik

Title: d'Arbeloff Assistant Professor of Mechanical Engineering

(This page is intentionally left blank)

Acknowledgements

﴿رَبِّ أَوْزِعْنِي أَنْ أَشْكُرَ نِعْمَتَكَ الَّتِي أَنْعَمْتَ عَلَيَّ وَعَلَى وَالِدَيَّ وَأَنْ أَعْمَلَ صَالِحًا تَرْضَاهُ﴾

I am extremely grateful to my advisor, Prof. Rohit Karnik, for his continued guidance and support, academically and personally, over the past two and a half years. Rohit, your hard-work and passion for research have really been a source of inspiration for me, and I truly appreciate all the time, patience, and genuine care you invested in me, for me to become a better researcher, and more importantly, a better person.

I also consider myself very lucky to having been part of a very talented and harmonious group of colleagues in the Karnik Lab – Yi-Heng Sen, Suman Bose, Chia-Hua Lee, Jongho Lee, Marco Cartas, Pam Basto, Pedro Valencia, Tarun Jain, Sean O'Hern, Dr. Minsoung Rhee, and Thea Szatkowski. You have all contributed to my learning and to making my MIT experience a personally enjoyable one. Special thanks are due to my project-mate and friend, Mr. Marco Cartas, for his fruitful collaboration in general and his help with the gelatin experiments in particular. I also wish to express my gratitude to Leslie Regan and Joan Kravit in the Mechanical Engineering department, for they have been the best allies a graduate student could have, and Kurt Broderick at the Exploratory Materials Laboratory (EML) for his guidance with the microfabrication processes.

I am very grateful to the Fulbright program at the U.S. Department of State for funding my studies at MIT, allowing me to venture into a new field, and making the work presented in this thesis possible.

No journey is devoid of ups and downs, and I have been blessed with a very special group of friends, here in Boston and in Cairo, whose presence and support made the ups more enjoyable and the downs more endurable. I'm lucky to have you guys in my life, and you have all my love and gratitude.

Finally, and most importantly, to my family – Mom, Dad, Cherine, Amr, and little Nour, I don't think I can thank you enough, but I know that this work and this entire journey wouldn't have been possible if it weren't for your unbounded love, support, and encouragement. For that I will be forever grateful.

Mohamed Raafat
Cambridge, Massachusetts
August 2010

(This page is intentionally left blank)

Table of Contents

List of Figures

List of Tables

(This page is intentionally left blank)

Chapter 1

Introduction

The ability to sort micron-sized cells, droplets, and particles, into distinct populations based on a given criterion is a very powerful and indispensible tool in a wide range of applications, including healthcare, research, and industrial applications.

In healthcare, cell sorting is of great significance, since several diseases have been found to alter the physical properties of cells [1-4]. For example, normal red blood cells typically have a biconcave disc shape 7-8 μm in diameter and 2-3 μm thick, and are deformable enough to squeeze into the smallest blood vessels, approximately 5 μm in diameter. However, once a cell gets infected with one of the malaria plasmodium parasites, it becomes much more rigid and unable to circulate in the narrow capillaries, which can eventually lead to the blockage of these capillaries [5, 6]. Similarly, sickle-cell disease reduces the deformability of red blood cells [7, 8], and sepsis is associated with a reduction in the deformability of both leukocytes and red blood cells [9, 10]. Epithelial cancer cells have been found to be larger in size and possess a different deformability compared to normal leukocytes [4, 11], which may aid in the isolation of these rare circulating tumor cells from blood.

Therefore, in these and other cases, the ability to differentiate between cells based on physical characteristics, namely size and deformability, can provide a powerful diagnostic tool for specific diseases. Moreover, experimental results suggest that assessing cell deformability can provide a good measure of disease progression in the case of malaria [12] and breast cancer [13].

Cell sorting is also critical in biological and biomedical research, where separation of specific cell populations from a heterogeneous mixture is necessary, e.g., for drug discovery experiments, and for fundamental studies on cell biology [14].

Aside from cells, the rapid development in droplet-based microfluidics enabled researchers to use micron- and sub-micron-sized droplets in a wide array of applications: they are used as chemical microreactors, holding very small quantities (femtoliters to microliters) of reagents, allowing for precise control over reaction timing and reagent mixing, and providing the ability to synthesize and transport solid reagents and products [15, 16]. Droplets are also used to encapsulate many biological entities, such as cells and proteins, for biomedicine and biotechnology applications [16].

A necessary complement to the use of droplets in these applications is the ability to probe and sort the droplets [17]. Sorting based on size and composition is necessary to ensure that the droplets being used as microreactors or to encapsulate biological particles satisfy precise volume and composition requirements, or to selectively remove specific droplets, e.g., from the products of a reaction, for further analysis or in search for a specific event [17].

Droplets are commonly used in pharmaceutical, cosmetic, food, and material industries to synthesize drugs, creams, and particles [18, 19]. Therefore, sorting has a significant role inensuring the uniformity of emulsions used, in order to guarantee a consistent product quality [20].

1.1 Existing Sorting Technology

Fluorescence-activated cell sorting (FACS) is still considered the method of choice for many biological applications [21] for sorting cells based on a large number of parameters including immunological and non-immunological (physical) characteristics such as size and density. Deformability, however, is not one of the parameters that can be readily measured using existing FACS machines.

Conventional techniques for assessing cell deformability include micropore filtration [22, 23], in which deformability is measured by the time taken for a cell sample to pass through a filter with known pore size, and ektacytometry [24], where a cell sample is sheared between two counter-rotating plates and resulting deformation is measured – both methods yielding a measure of the average deformability of the sample. However, it has been found that the results of such "bulk measurement" methods can be significantly skewed by the presence of a different cell type

in the sample [25, 26] or even a small subpopulation of the same cell type featuring different deformability [27]. Therefore, deformability measurement on the single cell level is necessary to identify different cell subpopulations and detect rare cells in a sample (e.g., circulating tumor cells in whole blood). In this aspect, micropipette aspiration [28, 29] stands out as the leading technique, in which part of the cell or the entire cell is sucked into a micropipette and ensuing deformation is analyzed. This technique yields excellent results in characterizing individual cells; however, it is not amenable to automation or high-throughput operation, due to limitations on the fabrication reproducibility of micropipettes, their susceptibility to breakage or blockage, and the dependence of the technique on operator skill [30].

The advances in microfabrication technology and microfluidics [31] have allowed for a new generation of sorting technology that combines the advantages of continuous operation with the small size scale suitable for probing and manipulating cells on the single cell level. Microfluidic cell sorting platforms require a smaller sample size, thereby reducing the cost of reagents, the analysis time, and most importantly, the invasiveness to patients when extracting the sample (e.g., blood) [21]. Finally, the small size of the devices combined with the relatively low cost to build them allow for massive parallelization, making high-throughput sorting in microfluidic devices a possibility.

Microfluidic sorting techniques which rely on physical characteristics as sorting criteria can be broadly classified into passive techniques and active techniques [21]. As the names imply, passive techniques rely solely on the interaction between the particles to be sorted, the geometry of the sorting device, and the characteristics of the flow; while active techniques rely on an externally-applied force field to perform the sorting.

Passive techniques include filtration through pillar and weir structures [32-34], inertial focusing [35, 36], pinched flow fractionation [37], and hydrodynamic filtration [38-40]. All passive techniques share the advantage of having relatively simple design and method of operation. However, it is not usually possible to change the sorting parameter or the sorting threshold in these devices without redesigning the sorting device.

Active sorting techniques typically use electric fields to manipulate cells and droplets, e.g., using dielectrophoresis [41, 42], or electrophoresis [43]. Optical force has also been used to switch cells and particles between two output streams [44, 45].

Guck *et al.* [13] have used optical tweezers to assess the deformability of cells in microfluidic channels, but without actually sorting them; and Rosenbluth *et al.* [27] measured the single-cell transit times of blood cell populations passing through a network of bifurcating microchannels, and used the information to establish the link between transit time distributions, cell deformability, and their diseased state [46].

1.2 Proposed Approach

In this work, we develop a microfluidic circuit that can perform passive, continuous sorting of cells and droplets based on the hydrodynamic resistance they induce as they pass through a microchannel. The hydrodynamic resistance of a particle, i.e., the resistance it induces to fluid flow in a channel, is directly related to its physical properties, such as size and deformability. To our knowledge, this is the first technique to use the hydrodynamic resistance induced by a particle as the mechanism that induces the sorting.

1.3 Thesis Layout

Chapter 2 explains the theoretical background and the device design process. Chapter 3 outlines the experimental setup and method used. The experimental results are given in Chapter 4, and Chapter 5 summarizes the results and suggests future directions.

Chapter 2

Theoretical Base and Device Design

In low Reynolds number flows, it has been observed that when a droplet traveling close to the center of a microchannel encounters a symmetric bifurcation, it either breaks at the junction or follows the path with the highest instantaneous flow rate [47, 48]. This phenomenon occurs due to the asymmetry in viscous forces acting on the droplet at the bifurcation: when the net viscous force acting on the droplet is balanced by the surface tension holding it together, the droplet follows the direction of the net viscous force, which – in the case of a symmetric geometry – acts in the direction of the branch with the higher velocity, hence flow rate. Conversely, when the net viscous force exceeds the surface tension, the droplet breaks at the junction [38, 48, 49]. This mechanism has been used to selectively split and sort droplets [38, 48, 50] and bubbles [51].

We capitalize on this phenomenon to sort deformable particles by designing a microfluidic circuit in which the flow rates in the branches of a Y-junction are dynamically set according to the hydrodynamic resistance induced by the particle as it flows through the circuit. The resulting modulation of flow at the junction switches the particle into one of two output channels, depending on the resistance it induces, which correlates with the physical properties of the particle in question (e.g., size, viscosity, deformability, etc.).

2.1 Working Principle

Figure 2.1 shows a schematic of the sorting circuit showing its main components and the flow rates therein: an input channel splits into two output channels (upper and lower) at a locally symmetric junction. The input channel is connected to one of the output channels via a 'bypass channel', and the portion of the input channel immediately preceding the sorting junction is the 'sensing channel'.

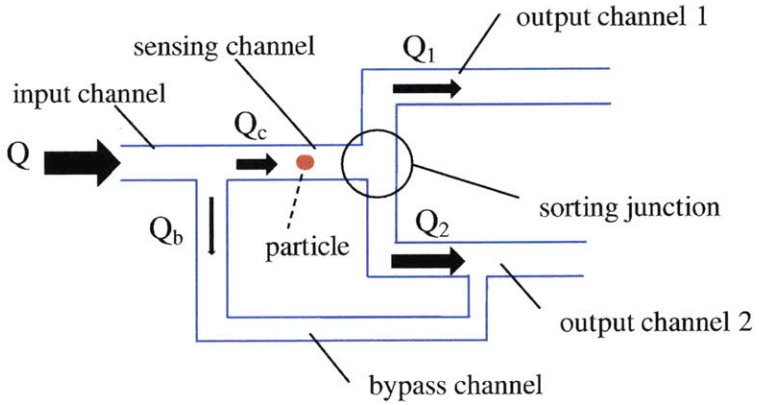

Figure 2.1 Sorting device – black arrows indicate flow rates.

Deformable particles are assumed to be dispersed in a carrier fluid and introduced through the input channel and into the sensing channel. A portion of the carrier fluid is diverted through the bypass channel and into the lower output channel. The amount of fluid being diverted is directly proportional to the hydrodynamic resistance induced in the sensing channel, e.g., as a result of a particle traveling in the channel and constricting the flow. The bypass channel thus acts as a feed-forward path, modulating the flow rates in the output channels according to the hydrodynamic resistance induced by the particle in the sensing channel.

According to this paradigm, design criteria could be set such that the baseline flow rate (in the absence of any particles) in the lower output channel is sufficiently higher than that in the upper output channel, we refer to this condition as the output flow being biased towards the lower channel. A particle of relatively low hydrodynamic resistance entering the sensing channel will divert more fluid into the lower output channel, causing the flow rates in both output channels to change, but not enough to disturb this bias. As the hydrodynamic resistance of the particle in the sensing channel increases, so will the amount of fluid being diverted through the bypass channel, until a certain threshold resistance where the flow rate in the upper channel will exceed that in the lower channel, and the bias will be reversed. Therefore, a particle that induces a resistance higher than the threshold resistance will be sorted into the upper channel, while a particle with a resistance less than the threshold resistance will be sorted into the lower channel. We note, however, that for the sorting action to happen, the particle needs to be relatively centered in the sensing channel, in order for it to experience the net shear force directing it to the

corresponding output channel. Consequently, very small particles that are not centered in the channel will follow the streamlines of one of the bifurcating flows into the respective output channel, and therefore will not be sorted by this mechanism, as was shown in [38].

2.2 Circuit Design

In order to design the microfluidic circuit to yield the desired sorting behavior, we note that at low Reynolds number, the steady-state, pressure-driven flow in a microfluidic channel is governed by the Stokes equation:

$$\nabla p = \mu \nabla^2 v . \tag{2.1}$$

The Stokes equation is integrated under the appropriate boundary conditions to yield the Hagen-Poiseuille law, governing the relation between the pressure difference Δp and the flow rate Q in the channel. The relation takes the general form

$$\Delta p = R_{hyd} Q , \tag{2.2}$$

where the proportionality constant R_{hyd} is the hydrodynamic resistance of the channel, which represents the pressure drop due to viscous dissipation in the channel, and can be shown to depend on the geometry of the channel and the viscosity of the fluid [52]. The Hagen-Poiseuille law is analogous to Ohm's law which relates the potential difference ΔV to the current passing in a conductor I through the resistance of the conductor R,

$$\Delta V = RI . \tag{2.3}$$

We make use of this analogy between microfluidic and electrical systems to create and analyze a simplified model of the proposed microfluidic circuit, in order to identify and design for the key parameters of the system, and gain some insights on its expected behavior.

2.2.1 Electrical domain

Figure 2.2 shows the equivalent electric circuit, where the flow rates in the channels, the pressures applied at the inlets and outlets, and the hydrodynamic resistances of the channels, are substituted by electric currents, voltage sources, and electrical resistances, respectively.

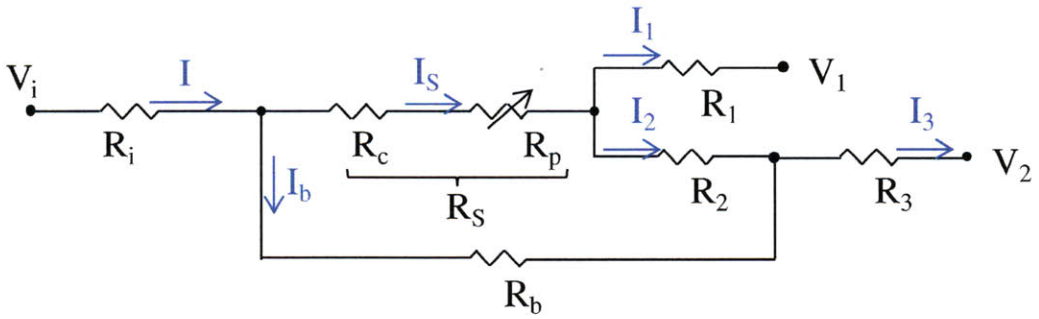

Figure 2.2 Electrical representation of the microfluidic circuit

We note, however, that this electric model has its limitations in that only the resistive elements of the circuit are being considered, while none of the capacitive elements are accounted for. The capacitance in the system could be due to the compliance of the channel walls, as well as to the compressibility of the fluid. We are also neglecting any dynamic effects in the system by considering only its steady state behavior. Nonetheless, our aim is to obtain an initial estimate for the system parameters and its expected behavior, and more detailed modeling and simulations can follow.

We assume a voltage-controlled circuit, and the objective is to solve for the currents in the different branches of the circuit as functions of the resistance in the sensing channel (R_S). This resistance will have a constant part (R_c) and a variable part (R_p), which in the original system correspond to the resistance of the unobstructed channel, and the additional resistance due to the presence of a particle partly obstructing the flow, respectively, such that

$$R_S = R_c + R_p. \tag{2.4}$$

We simplify the circuit by noting that the delta connection (emphasized in Figure 2.3) can be simplified using the Y-Δ transformations into the circuit shown in Figure 2.4, with the corresponding resistances given by:

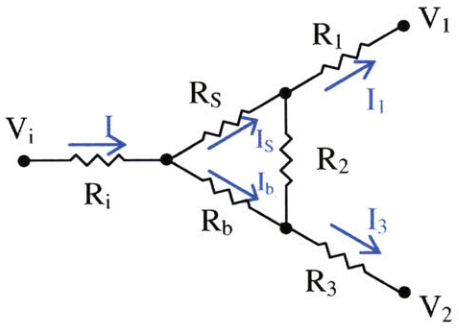

Figure 2.3 Delta connection

$$R_X = \frac{R_S R_b}{R_S + R_b + R_2}$$

$$R_Y = \frac{R_S R_2}{R_S + R_b + R_2} \qquad (2.5)$$

$$R_Z = \frac{R_b R_2}{R_S + R_b + R_2}$$

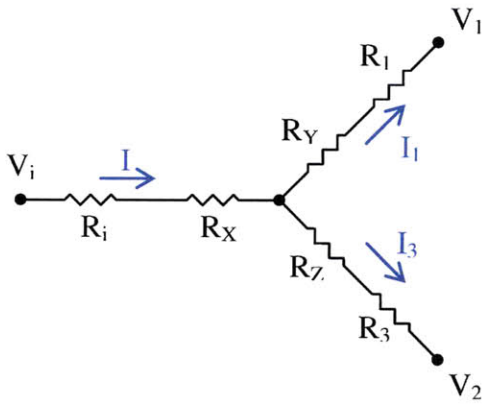

Figure 2.4 Y- connection

Combining the resistances connected in series yields the Y-connection shown in Figure 2.5, with the corresponding resistances given by:

$$R_\lambda = R_X + R_i$$
$$R_\mu = R_Y + R_1 \qquad (2.6)$$
$$R_\Delta = R_Z + R_3$$

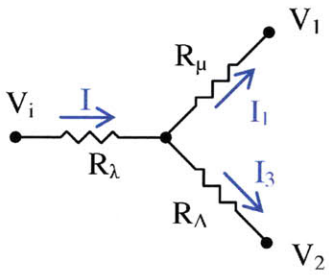

Figure 2.5 Simplified circuit

Solving for the currents in the simplified circuit, then back-substituting in the original circuit, we obtain the currents in all branches:

$$I_1 = \left[V_i - V_2 + (V_2 - V_1)\frac{R_\lambda + R_\Delta}{R_\Delta} \right] \cdot \frac{R_\Delta}{R_\lambda R_\Delta + R_\Delta R_\mu + R_\mu R_\lambda}$$

$$I_3 = \frac{V_1 - V_2}{R_\Delta} + \frac{R_\mu}{R_\Delta} \cdot I_1$$

$$I_2 = \frac{V_1 - V_2 + I_1 R_1 - I_3 R_3}{R_2} \qquad (2.4)$$

$$I = I_1 + I_3$$

$$I_b = I - I_1 - I_2$$

$$I_S = I_1 + I_2$$

We note that the all currents are in fact functions of the resistance in the sensing channel, R_S, as well as all the other circuit parameters, namely the resistances (R_1, R_2, R_3, and R_b), and the applied voltages (V_i, V_1, and V_2).

Due to the large number of parameters involved and the nonlinear functions governing the currents, we adopted a trial-and-error procedure to scan a portion of the parameter space for ranges of values that would yield the desired sorting behavior, namely a reversal in the output bias (I_1 vs. I_2) as R_S increases. Equations 2.5, 2.6, and 2.7 were programmed into MATLAB, and the flow rates were calculated as functions of R_S for different parameter configurations. Figure 2.6 shows the currents resulting from one such configuration, with the corresponding parameters listed in Table 2.1. We can see that there is a threshold value for the resistance R_S ($R_S = 4\ \Omega$), at which the output bias switches from one output branch to the other, specifically,

$$I_2 > I_1 \quad \text{for} \quad R_S < 4\ \Omega$$
$$I_1 > I_2 \quad \text{for} \quad R_S > 4\ \Omega$$

V_i [V]	1
V_1 [V]	0
V_2 [V]	0
R_i [Ω]	10
R_b [Ω]	6
R_1 [Ω]	6
R_2 [Ω]	1
R_3 [Ω]	2

Table 2.1 Circuit parameters corresponding to Figure 2.8

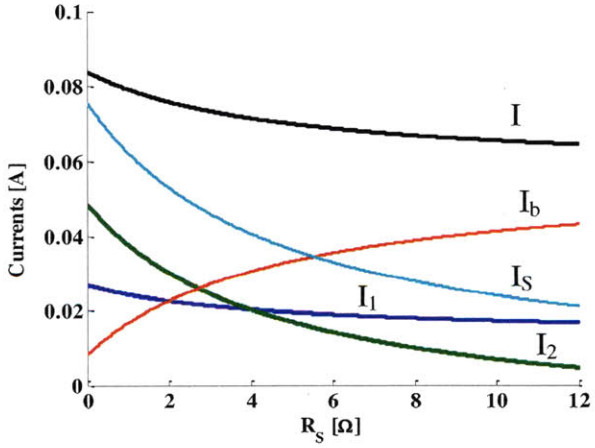

Figure 2.6 Circuit currents as function of channel resistance

2.2.2 Microfluidic domain

Once parameters were found in the electric domain that yielded the desired switching behavior, we are now faced with the task of translating these parameters into the physical, microfluidic domain. In order to do that, we first note that the hydrodynamic resistance of a channel (R) is obtained – as we previously mentioned – by integrating the Stokes equation (2.1)

with the appropriate boundary conditions. For square and rectangular channel cross-sections, the hydrodynamic resistances can be approximated by [52]:

$$R = \frac{12\mu L}{1-0.63(h/w)} \cdot \frac{1}{h^3 w} \quad \text{for a rectangular microchannel, and by} \tag{2.8}$$

$$R = 28.4\frac{\mu L}{h^4} \quad \text{for a square micrchannel,} \tag{2.9}$$

where μ is the fluid viscosity, and L, w, and h are the channel's length, width, and height, respectively (with $h \leq w$).

In one design variation, we chose all channels to be square (20 μm x 20 μm); hence changing a channel's hydrodynamic resistance only entails changing its length. A few more iterations were necessary in order to meet two additional constraints imposed on the device, namely that the flow rate in the bypass channel had to be lower than that in the sensing channel, in order to drive the incoming particles into the sensing channel and not the bypass channel; and that the designed channel lengths had to be experimentally realizable.

We settled on the geometry shown in Figure (2.7). Using these dimensions, and setting the input pressure at 10 kPa, both output pressure at zero, and assuming oil (with density ρ = 850 kg/m^3, and viscosity $\mu = 10^{-2}$ Pa·s) is flowing in the channels, we used MATLAB to calculate the flow rates in the channels as functions of the R_S. The results are plotted in Figure 2.8 (left).

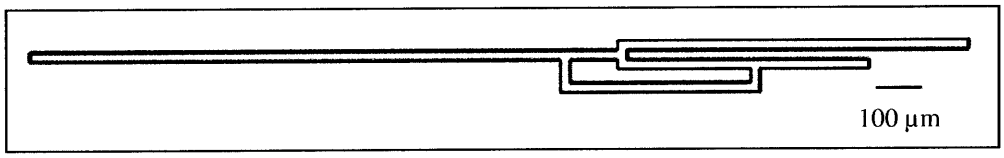

Figure 2.7 Top view drawing of the sorting device

We first note that the flow rates in the channels are on the order of 0.1 μL/min, which yield average flow velocities on the order of 10^{-2} m/s. This yields a Reynolds number (equation 2.10) on the order of 10^{-2}, signifying that the inertial forces are negligible compared to the viscous forces, and justifying the use of the Stokes equation (equations 2.1) to describe the flow in channels.

$$\mathrm{Re} = \frac{\rho v D_h}{\mu} \tag{2.10}$$

Paying a closer look at the flow rates, we can see that when the sensing channel is free from particles (R_S=R_c=1.78x10^{14} Pa·s/m^3), the flow rate in the sensing channel is significantly higher than that in the bypass channel ($Q_c > Q_b$), ensuring that particles will not flow into the bypass channel. In this (unobstructed) case, the flow rates in the upper and lower channel are found to be:

$$Q_1 = 0.086\ \mu\text{L/min, and}$$

$$Q_2 = 0.091\ \mu\text{L/min.}$$

We note that $Q_2 > Q_1$. We define the bias ratio $\beta = \frac{Q_2}{Q_1}$; in this case β = 1.06, and the output is said to be biased downwards.

As the resistance in the sensing channel R_S increases, the flow rates in the output channels vary gradually causing the bias ratio to decrease; however, the downward bias ($\beta > 1$) is maintained until the resistance in the channel reaches the threshold resistance ($R_S = R_{th}$ = 2.5x10^{14} Pa·s/m^3), at which point the flow rates in both channels are equal (β = 1). As R_S increases further beyond R_{th}, the output becomes biased upwards, and the bias ratio β drops below 1.

The fashion in which the model responds to changes in R_S gives rise to two operating regimes, namely region I and region II, depicted in Figure 2.8. In region I, a particle with a relatively low hydrodynamic resistance traveling close to the center in the sensing channel will cause the total resistance (R_S) to rise, but not beyond the threshold value ($R_c < R_S < R_{th}$), hence maintaining the downward bias and leading the particle to exit along the lower channel. Conversely, in region II, a particle causing the total resistance to exceed the threshold resistance ($R_S > R_{th}$) will cause an upward bias, and will exit along the upper channel. The schematics in Figure 2.8 (right) depict the expected behavior in each case.

This predicted performance suggests that passive sorting of particles could be realized, with only the hydrodynamic resistance of the particles dictating their exit paths.

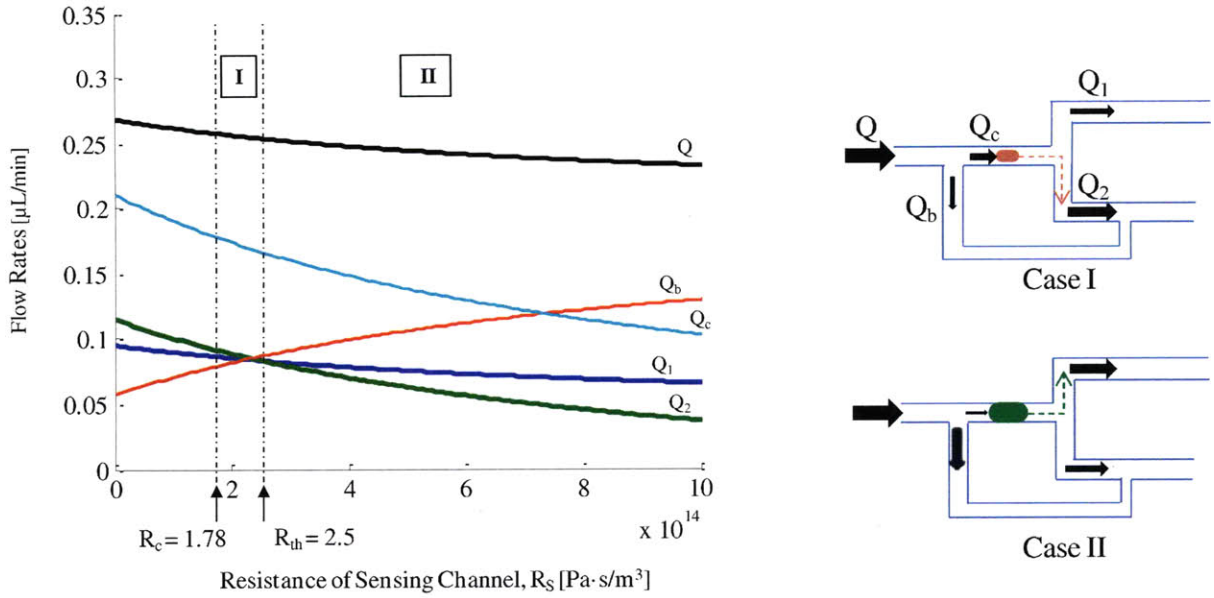

Figure 2.8 Effect of sensing channel resistance on flow rates (left), and the expected sorting behavior (right) – black arrows' sizes illustrate relative flow rates in the channels; colored dashed arrows indicate the path of the particles.

2.3 Effect of Output Pressure

We note that the threshold resistance can be adjusted by applying pressure at the outlets. Figure 2.9 shows the effect of applying a pressure of 200 Pa (2% of the input pressure) at one of the outlets while keeping the pressure at the other outlet at zero. In the first case, the pressure is applied at the upper outlet while the pressure at the lower outlet is kept at zero (Figure 2.9 a). We notice that the threshold resistance nearly doubles to 4.4×10^{14} Pa·s/m^3, which means that the particle size inducing switching – the cutoff size – will increase accordingly. In the second case, the pressure is applied at the lower outlet, while the pressure at the upper outlet is kept at zero (Figure 2.9 b). In that case, the threshold resistance decreass to 1.1×10^{14} Pa·s/m^3, which is less than the resistance of the unobstructed channel ($R_{th} < R_c$). This means that that the flow will always be biased upwards regardless of the presence or the resistance of a particle in the sensing channel, and no switching or sorting will occur. Therefore region I disappears, and region II spans the entire operating range ($R_S \geq R_c$).

This ability to adjust the threshold resistance provides a simple means of tuning the sorting cutoff without having to modify the device geometry. This opens the door to being able to use the same device for sorting of different types of particles, or to use the same device for multi-step sorting of the same type of particles.

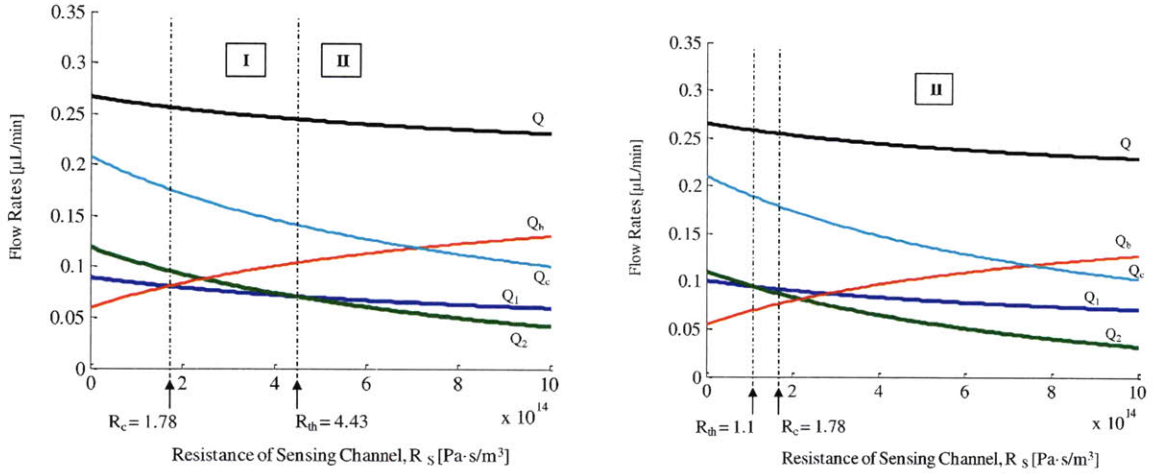

Figure 2.9 Effect of output pressure on device performance. (a) 200 Pa applied at upper output channel, and (b) 200 Pa applied at the lower output channel.

2.4 Numerical Simulations

We used COMSOL Multiphysics, a finite element analysis package, to simulate the flow in the proposed circuit. By incorporating the detailed device geometry into the model, this analysis aims at validating the results obtained using the electric circuit model, and providing more accurate quantitative estimates of how the device would perform under different operating conditions.

A 3D geometric model of the circuit, shown in Figure 2.10, was constructed. Pressure boundary conditions were applied at the inlet and two outlets, and no-slip boundary conditions were applied at all other boundaries. An appropriate mesh was selected, and the Stokes flow model was employed to describe the steady-state, predominantly viscous flow in the channels. Solving for the velocity distribution in the channels, the solution in Figure 2.11 is obtained,

depicting the velocity distribution at the mid-plane of the device (z = 10 μm), when all channels are free from particles.

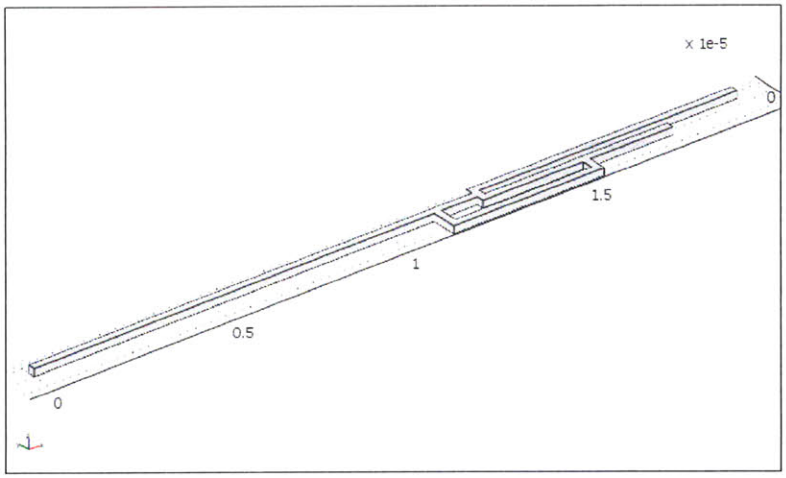

Figure 2.10 Geometric model of the microfluidic circuit

The velocities obtained were on the same order of magnitude (10^{-2} m/s) predicted by the electric circuit model. The maximum flow velocities in the sensing and bypass channels were 12.7 mm/s and 6.9 mm/s, respectively. The maximum flow velocities in the lower and upper channels are found to be 7.1 mm/s and 5.8 mm/s, respectively, which yields a bias ratio $\beta = 1.23$. The bias ratio is approximately 16% higher than the one predicted using the electric circuit model. We believe this minor discrepancy could be attributed to the approximation used when calculating the hydrodynamic resistance of the channels (equation 2.9), and any effects arising from the junctions and the corners, that were not included in the model.

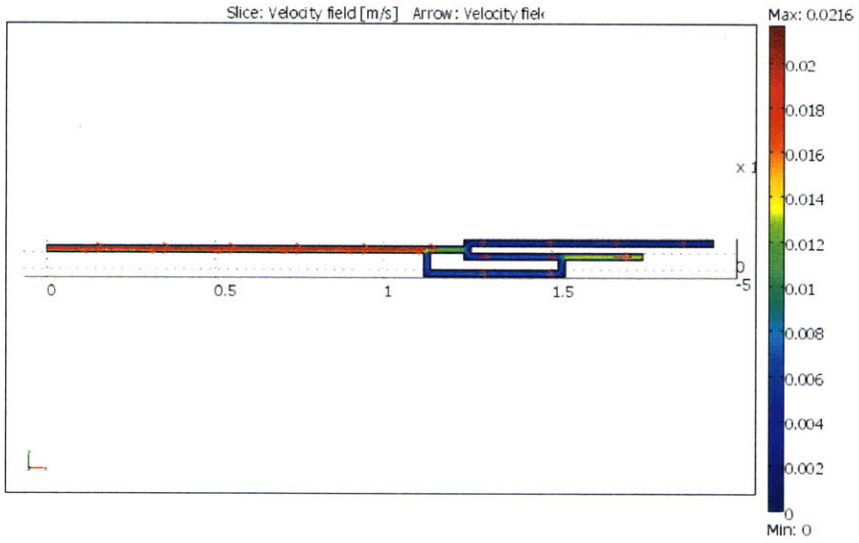

Figure 2.11 Simulated velocity distribution in the unobstructed channels

Next, we introduce an obstruction in the sensing channel to simulate a resistance and observe its effect on the output flow rates. Figure 2.12 shows the velocity profile when a solid sphere of diameter 10 μm is centered in the sensing channel. We find the maximum flow velocity decreasing in the sensing channel to 11.5 mm/s, and increasing in the bypass channel to 7.75 mm/s as more flow is being diverted from the sensing channel, and the velocities in both the upper and lower channels decreasing, to 5.6 mm/s and 6.6 mm/s, respectively, which reduces the bias ratio to $\beta = 1.18$. When the diameter of the sphere reaches 15 μm, the velocities are almost equal in both channels – this is the threshold (cutoff) size. When the sphere diameter increases to 16 μm (Figure 2.13), the maximum flow velocities in the output channels decrease further to 4.6 mm/s and 4.4 mm/s in the upper and lower channels, respectively, causing the bias ratio to dip below one to $\beta = 0.96$, switching the bias to the upper channel.

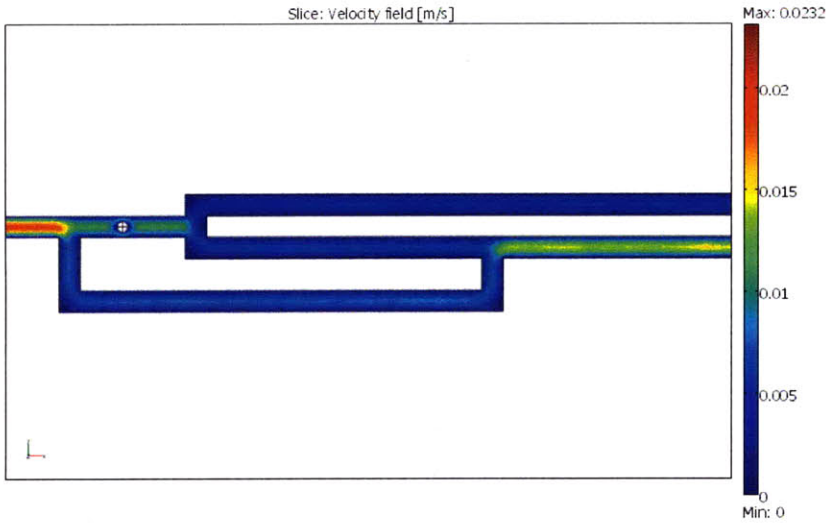

Figure 2.12 Simulated velocity distribution with a 10 µm obstruction in the sensing channel

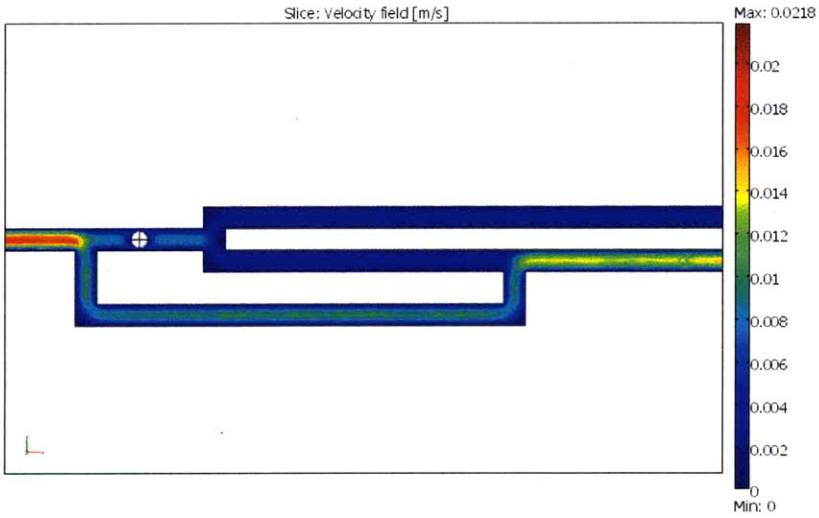

Figure 2.13 Simulated velocity distribution with a 16 µm obstruction in the sensing channel

2.5 Dynamic Effects

We note that both the resistance and the numerical models are steady-state models and do not take into consideration the dynamics of the flow. In order to study the effect of flow dynamics on the sorting characteristics, we need to consider the relationship between the time scales relevant to the sorting process, namely, the transit time of the particle in the channels and the inertial time scale τ_i required to establish steady flow in the channel [53], which is given by

$$\tau_i \sim \frac{\rho L_0^{\,2}}{\eta} \tag{2.11}$$

where L_0 is the length scale of relevance if the channel. Therefore, if the particle transit time in the channel is less than the time constant of the flow, then the flow will not have sufficient time to respond to the perturbation caused by the presence of the particle, and sorting may not occur. In our model, a channel with a length scale on the order of 10 μm filled with oil (ρ = 850 kg/m^3, $\mu = 10^{-2}$ Pa·s), will have an inertial time constant $\tau_i \sim 10$ μs. Therefore if the particle transit time in the channel is less than 10 μs, the flow rates might not be adequately perturbed by the time the particles exits the sensing channel. This also means that the particle has to spend less than 10 μs at the junction, otherwise the flow rates will return to their unperturbed state, and sorting would be hindered.

Chapter 3

Experimental Setup

3.1 Device Fabrication

The sorting devices were fabricated by molding in PDMS using SU-8 masters [54]. The process has been extensively described in the literature, and therefore will only be outlined below.

Figure 3.1 shows one of the 4-inch transparency masks used for the photolithography process. The different designs featured on the mask were drafted using a layout editor software (L-Edit), then plotted at high resolution (40,640 DPI) on transparency paper, with only the device areas clear and the rest of the mask dark.

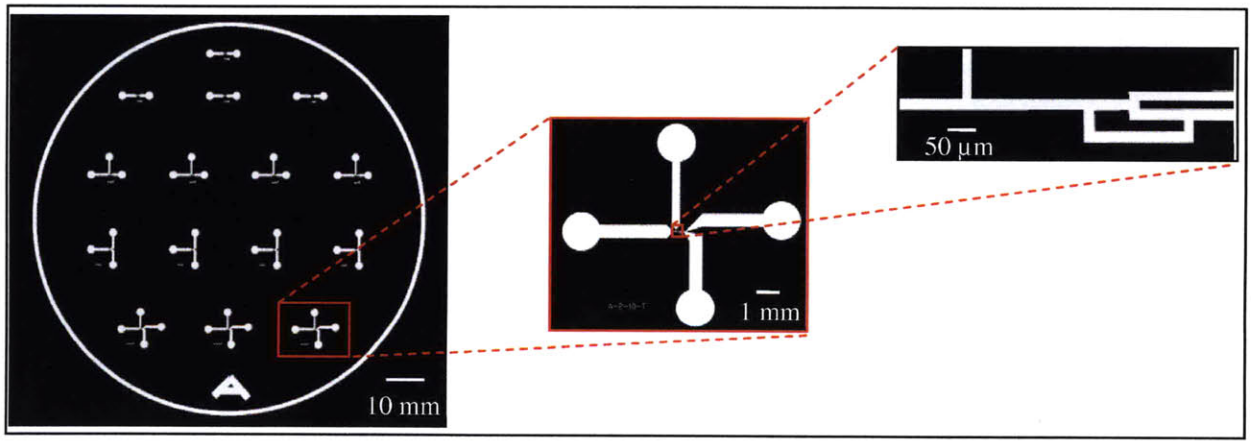

Figure 3.1 Transparency mask – magnified images show sorting device with droplet-generation T-junction

Microfabrication was carried out in the Exploratory Materials Laboratory (EML) facility at MIT. A layer of negative photoresist (SU-8 10, MicroChem Corp.) was deposited on a 4-inch Silicon wafer (Silicon Valley Microelectronics) by spin coating. The transparency mask was aligned to the wafer and the assembly exposed to UV light using a mask alignment-wafer expose

system (MJB-3, Karl Süss). The machine uses a 200 W mercury lamp and filters for wavelengths 365 nm and 405 nm, cross-linking the photoresist exposed through the mask's clear areas. The remaining photoresist is not cross-linked and is later dissolved using a developer (PM acetate). The wafer is rinsed with acetone, dried with Nitrogen, and is ready to act as the master mold for the subsequent casting process.

PDMS (Sylgard 184, Dow Corning) was acquired from Ellsworth Adhesives and mixed with its curing agent in a 10:1 ratio, degassed, and poured on the master wafer. The cast was heated in an oven for 45 minutes at 90°C to allow for the PDMS to cure. The cured PDMS was subsequently peeled from the wafer, holes (0.0145-in in diameter) were drilled into the PDMS using drill bits #79 to create the inlet and outlet ports, and the individual devices were cut, cleaned using scotch tape, thoroughly rinsed with acetone and isopropyl alcohol, and finally bonded to microscope glass slides using oxygen plasma etching, creating an irreversible bond. Figure 3.2 shows a schematic of the soft lithography process, and Figure 3.3 shows an image of a glass slide on which three devices are bonded.

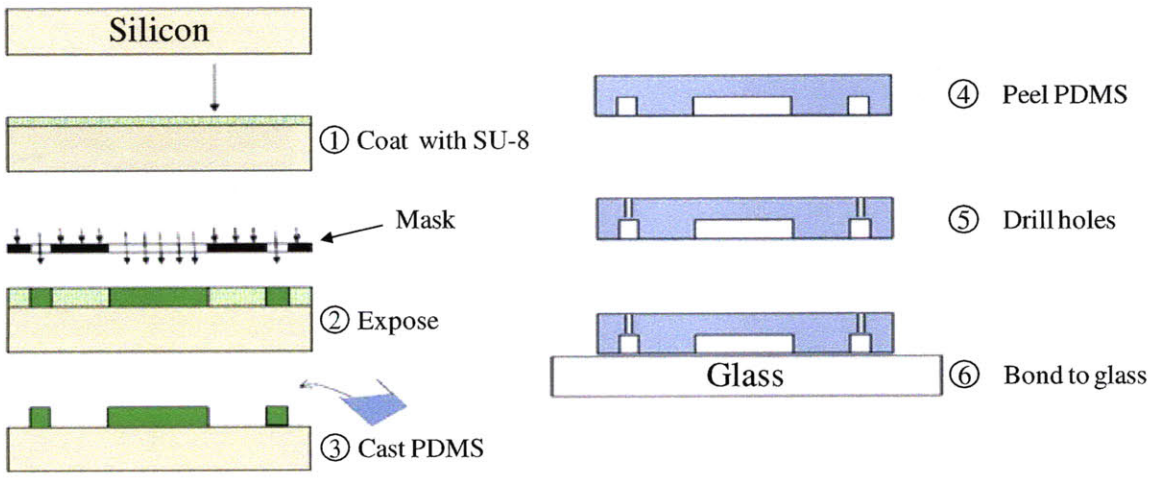

Figure 3.2 Schematic of the soft lithography process

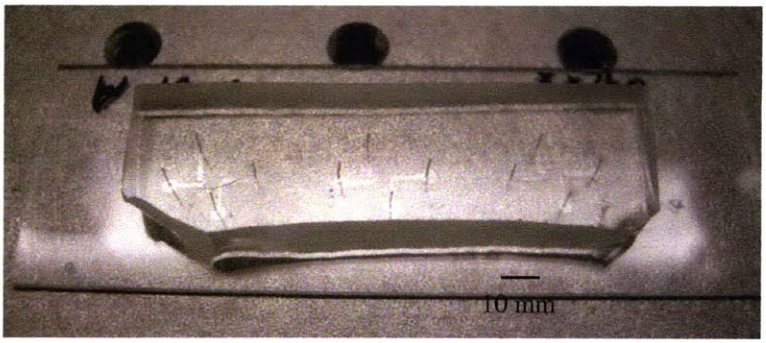

Figure 3.3 PDMS with three devices bonded to glass slide

3.2 Experimental Setup

Figure 3.4 shows the experimental setup used to conduct the sorting experiments in the laboratory. The microscope slide with the devices is mounted on a Nikon TE-2000U inverted microscope equipped with a CCD camera (iXon, Andor Technology). The fluids to be flown through the device are contained in 4-ml screw thread glass vials from VWR, and Tygon flexible tubing (0.012-in inner diameter, 0.016-in outer diameter) from Cole-Parmer carry the fluids to the device, by having one end submerged under the fluid surface and the other end inserted into the inlet ports on the device. A different set of Tygon tubes (0.02-in inner diameter), delivers nitrogen gas from a pressure source into the vials, pressurizing their content and driving the fluids into the device. The vial caps are of the open top type, with PTFE lining (both caps and lining were obtained from VWR), through which holes are drilled to allow for the tubes to go into and out of the vials. The holes are sealed by pouring molten wax on the top of the vial.

The flows are controlled by manually adjusting the nitrogen supply pressures for each fluid stream using a pressure monitoring and control unit built in the lab, consisting of pressure regulators (Bellofram, and Fairchild, both obtained directly from manufacturers), and pressure sensors (SSI Technologies) from McMaster-Carr. The outlet ports are connected to individual vials in the same manner, to collect the fluids exiting the device, and to apply pressure at the outlets as needed.

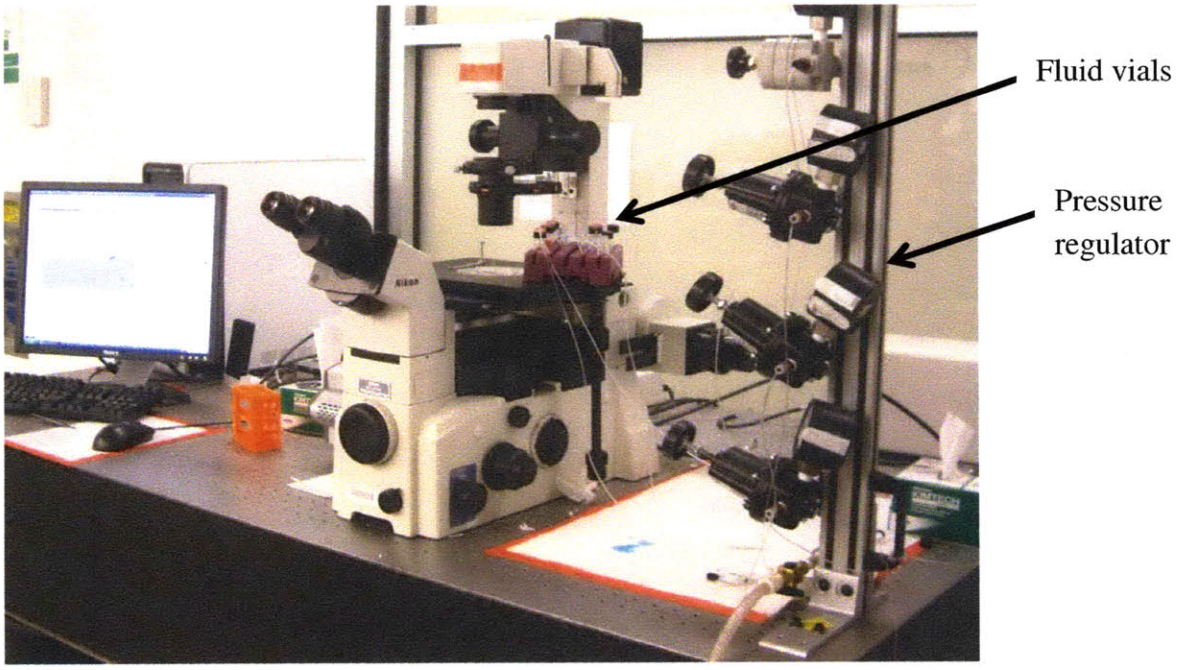

Figure 3.4 Experimental setup

3.3 Experiments Roadmap

To demonstrate sorting based on hydrodynamic resistance, two sets of experiments were planned. The first set involves the size-based sorting of deformable gelatin particles dispersed in a carrier fluid, where bigger particles are expected to induce higher hydrodynamic resistance than smaller ones. The second set involves the deformability-based sorting of droplets of different composition dispersed in a carrier fluid, where less deformable droplets are expected to induce a higher resistance than more deformable ones.

3.4 Materials and Methods

3.4.1 Continuous phase

Due to the hydrophobic nature of PDMS [55], we opted to use oil as the carrier fluid in both sets of experiments, and use water-based droplets and gelatin particles as the dispersed phases.

Light mineral oil (Mallinckrodt Chemicals) from VWR was used as the oil phase. A surfactant (Span 80, from Sigma-Aldrich) was added at 1% (w/v) to the oil to stabilize the droplets. Span 80 was chosen because it is a nonionic surfactant, with a hydrophilic-lypohilic balance (HLB) of 4.3, rendering it more soluble in the oil phase than in the aqueous phase [56]. The critical micelle concentration (CMC) of Span 80 in mineral oil is 0.025% (w/v); using a surfactant concentration greater than the CMC has the effect of reducing the interfacial tension between mineral oil and water from 0.05 N/m to 0.011 N/m [57], facilitating droplet breakup. The surfactant also stabilizes the droplets by absorbing on the water-oil interface, thus preventing the droplets from coalescing or wetting the channel walls.

3.4.2 Deformable gelatin particles

The deformable gelatin particles were synthesized by suspending a water-based gelatin solution in the oil phase. The gelatin solution was prepared by adding 0.05 g/mL gelatin from bovine skin (G9382, Sigma-Aldrich) to water (with 0.1 mg/mL Rhodamine Chloride or Patent Blue V Calcium Salt to facilitate imaging), followed by sonication, heating to 85°C, and stirring, to ensure complete mixing. 0.4% by volume of the solution was added to the oil-surfactant mixture, vortexed for 10 min, and stored at 4°C until used. The size of the particles could be controlled by adjusting the vortexing speed. Figure 3.5 shows a photomicrograph of gelatin particles synthesized using this method and dispersed in oil-surfactant mixture.

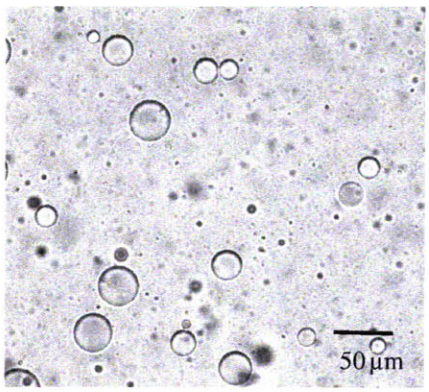

Figure 3.5 Gelatin particles in oil-surfactant. Figure courtesy of Mr. Marco Cartas.

In order to estimate the hydrodynamic resistance induced by the gelatin particles in the microchannels, we made use of the microfluidic differential manometer, presented by Howard Stone's group at Harvard University [58]. The device consists of two microfluidic channels with separate inlets and a common outlet, and two miscible, but distinguishable fluids are flown through the two channels, respectively, giving rise to an interface at the common outlet channel. The position of the interface can be calibrated by adjusting the supply pressures. Once the baseline position of the interface has been set, particles are introduced through one of the channels (the measurement channel) while the other one acts as a reference channel. As a particle goes through the measurement channel, it obstructs the flow inside that channel, and the interface in the output channel moves accordingly. With proper calibration, the changes in the interface position can accurately reflect the additional pressure drop, hence the hydrodynamic resistance, due to the presence of the particle in the measurement channel [58].

We designed and fabricated a number of manometers, with different channel dimensions. Figure 3.6 shows one such manometer, with a gelatin particle traveling in the upper (measurement) channel. The fluid in the upper channel is the oil-surfactant mixture used as the continuous phase in the sorting experiments, and that in the lower channel is the same mixture, but to which was added 0.1 mg/mL Patent Blue V Calcium Salt. The measurement and reference channels have a square cross-section, with a 20 μm side.

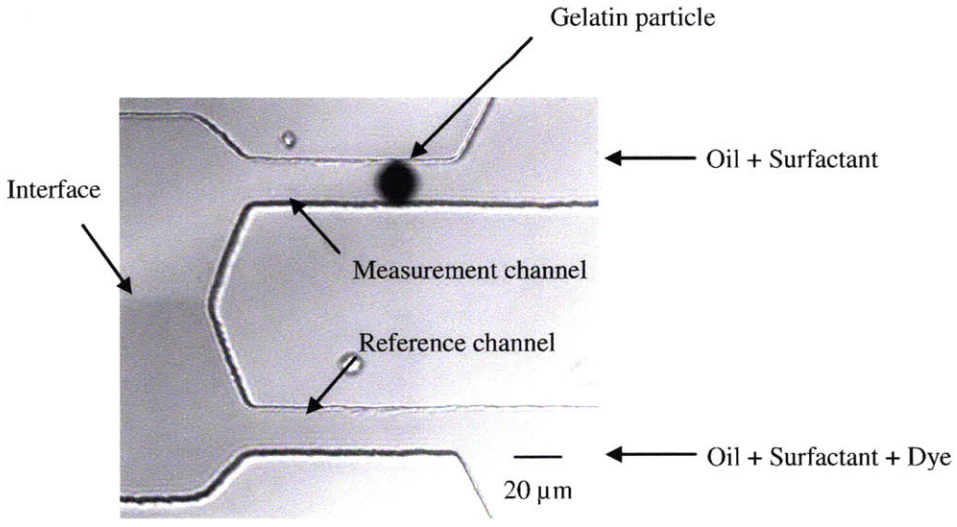

Figure 3.6 Microfluidic manometer with gelatin particle in measurement channel

3.4.3 Droplet generation

For the droplets experiments, we chose to use similar-size droplets of water and glycerol dispersed in the oil phase. Glycerol (BDH) was obtained from VWR, and DI water was supplied by a Millipore Direct-Q 3 UV unit, and the droplets were generated on the PDMS chip using two T-junctions upstream of the sorting circuit.

In this droplet generation technique, the discontinuous phase (water or glycerol) is introduced at a right angle into the continuous phase (oil/surfactant). When the pressure of the dispersed phase is lower than that of the continuous phase, monodisperse droplets are created as a result of the balance between the shear forces acting on the dispersed phase and the surface tension forces holding it together. The scaling relation yields the droplet radius r [59]:

$$r \sim \frac{\gamma}{\mu \dot{\varepsilon}} \tag{3.1}$$

where γ is the interfacial tension between the continuous and dispersed phases, μ is the viscosity of the continuous phase, and $\dot{\varepsilon}$ is the shear rate in the crossflow region, given by

$$\dot{\varepsilon} \sim 2\frac{\mathrm{v}}{\mathrm{H}} \tag{3.2}$$

where v is the flow velocity in the crossflow region and H is the channel height.

Therefore, by controlling the supply pressures of the continuous and dispersed phases, the droplet size and generation rate can be controlled. It can also be seen that using by Figure 3.7 shows the T-junctions and the two types of droplets.

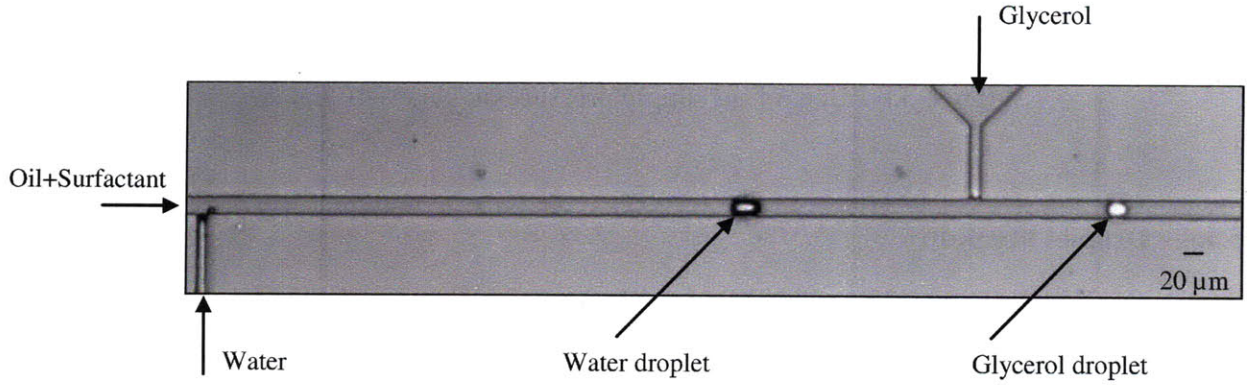

Figure 3.7 Photomicrograph of two microfabricated T-junctions generating droplets of water (left) and glycerol (right) in mineral oil/surfactant.

Table 3.1 and Figure 3.8 show the effect of changing the supply pressures of the oil and water streams, respectively, on the size of the water droplets. As the oil pressure increases, the droplet radius decreases, which could be explained in light of equation 3.1 as follows: as the oil pressure increases, the flow velocity increases, which increases the shear rate $\dot{\varepsilon}$, and reduces the droplet radius. We also note from equation 3.1 that using a surfactant, which reduces the interfacial tension, smaller droplets can be obtained.

Oil pressure (psi)	Water pressure (psi)	ΔP (psi)	Droplet diameter (um)
9	10.4	1.4	28
12	10	2	24
16.8	14	2.8	19
22.8	19	3.8	16

Table 3.1 Effect of supply pressures on water droplet size

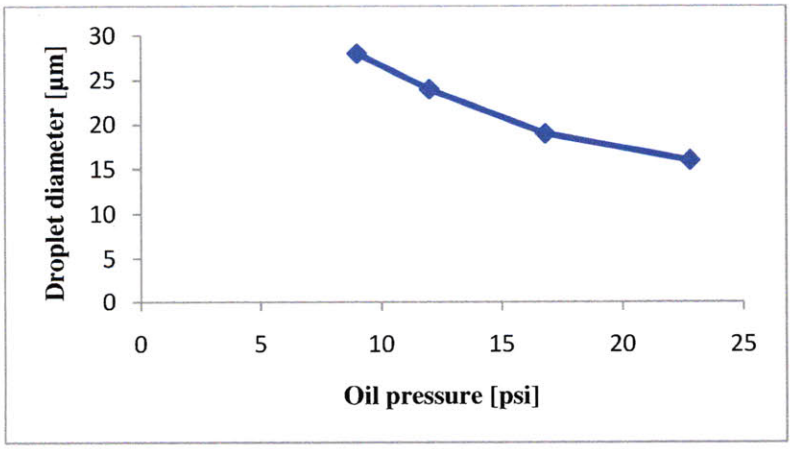

Figure 3.8 Effect of oil supply pressure on water droplet size

3.4.4 Droplet breakup

Link *et al.* [48] studied the breakup of droplets in microchannels as they reach a T-junction, and concluded that droplets break as a result of the Rayleigh-Plateau instability where a cylindrical liquid thread can reduce its total surface area by breaking when its height exceeds its circumference. They found that whether or not a droplet breaks as it reaches a symmetric T-

junction depends on its original dimensions, and the deformation rate to which it is subjected, with bigger droplets and those subjected to a higher deformation rate being more susceptible to break than smaller ones, or those subjected to a lower deformation rate, respectively.

They obtained the graph shown in Figure 3.9 experimentally, showing that droplets with a length-to-circumference ratio greater than one always break at the junction. Smaller droplets, however, only break when the capillary number of the flow exceeds a threshold value. The capillary number represents the ratio of viscous stresses to those due to interfacial tension, and is given by

$$Ca = \frac{\mu \cdot \mathrm{v}}{\gamma} \tag{3.3}$$

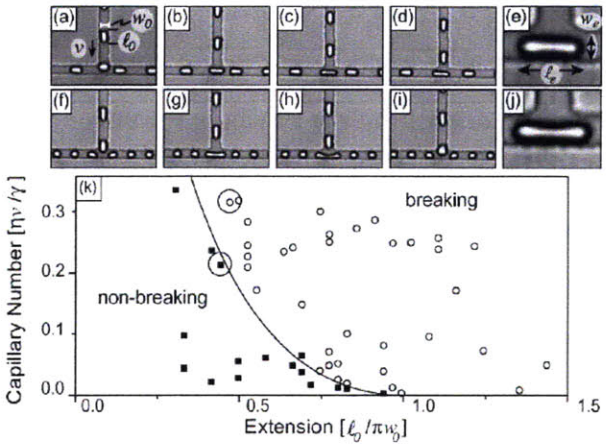

Figure 3.9 [48] Droplet breakup at a symmetric T-junction: a non-breaking drop is shown in (a-e), and a breaking drop shown in (f-j). The curve in (k) shows the critical boundary between breaking and non-breaking drops.

For our droplet experiments, we needed to be operating in the non-breaking regime. This meant working with droplets that have the ratio $\frac{l_0}{\pi w_0}$ less than 1, and operating at a capillary number below the critical value. Given our channel dimensions, the droplet length should not exceed 62 μm to prevent breakup. The typical droplet length in our devices ranged between 10-30 μm, which yielded a ratio of around 0.3, well within the breakup limit. Using the values obtained earlier for the flow velocities and properties of the oil used, the capillary number was

$$Ca \sim \frac{0.015 \times 0.1}{0.01} \sim 0.1$$

which means that the droplets should not break as they reach the sorting junction.

3.4.5 Channels and tubes degassing

Before sorting experiments could be carried out, the sorting channels and the tubes had to be free from air bubbles, to guarantee consistent results. The following procedure was thus followed: the tubes were initially disconnected from the device. The outlet vials – containing the same continuous phase to be used in the experiment – were pressurized until the tubes were completely filled with liquid and all air had been flushed out. The tubes were then connected to the outlet ports on the device, hence filling the device with the continuous phase and displacing the air towards the inlet ports, though which it exited the device. Once all air bubbles had exited, inlet vials were pressurized in the same manner to flush air from the tubes, which were then inserted into the inlet ports; at which time the tubes and channels should be free from air bubbles, and the pressures could be set at their operating levels.

Occasionally, some air bubbles would persist inside the channels after all tubes have been connected; in this case, a continuous application of pressure from all ports would force the bubbles to diffuse through the PDMS.

3.4.6 Flow visualization

In order to have a quantitative measure of the device performance, an accurate measurement of the flow velocities in the different channels is necessary. We adopted the particle streak velocimetry method (PSV) [60] to visualize and quantify the flow in the channels. Small, fluorescent particles were dissolved in the continuous phase, and successive images of the sorting circuit were acquired at high frame rate, where the particles would appear as small streaks due to their motion with the flow during the exposure time. By measuring and comparing the lengths of the streaks, one should be able to determine the flow velocities in the channels.

Figure 3.10 shows one of the images showing the fluorescent streaks in the sorting circuit taken at an exposure time of 6 ms.

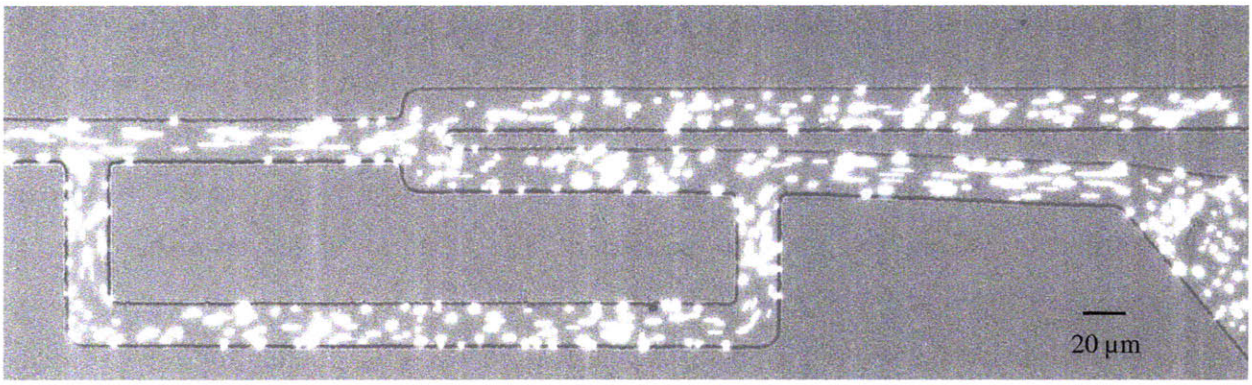

Figure 3.10 Fluorescent streaks in the channels

We chose to use 1-μm fluorescent microspheres as flow tracers: they are sufficiently small to provide a good representation of the flow velocities in the 20 -μm channels, while being large enough to generate a strong scattering signal for good visualization. However, none of the commercially available microspheres could be readily used: hydrophobic microspheres (e.g., polystyrene) would stick to the channel walls and not flow, while hydrophilic ones (e.g., sulfate- or carboxylate-coated microspheres) would typically adhere together, creating large clumps, and blocking the flow.

To enhance the dissolution of microspheres in mineral oil, composed mainly of long alkane chains, we coated the microspheres with a compound that features long aliphatic hydrocarbon chains. We used n-octadecyltrimethoxysilane from Gelest to coat polystyrene microspheres. We chose to use polystyrene microspheres since their density (1050 kg/m^3) was closer to that of the oil (850 kg/m^3) than that of the silica particles (approx. 2000 kg/m^3); hence they have a better ability to follow the flow. The following protocol was used to coat the microspheres:

1-μm, fluorescently-labeled, carboxyl-coated, polystyrene microspheres were acquired from Invitrogen. They were provided at an initial concentration of 2% solids in a water solution. We aimed at having approximately 10 spheres in a 20 μm x 20μm x 100 μm volume, to provide a good distribution in the channel while allowing for easy visualization. The target concentration

was then calculated approximately to be 0.01% solids, which meant the solution had to be diluted 200 times.

The microspheres were initially washed in ammonium hydroxide (Sigma-Aldrich), diluted to a final concentration of 15% ammonia in water, then rinsed with DI water twice, then with ethanol once, where after every wash the solution was centrifuged, and the supernatant pipeted out. After the three washes, ethanol was added to the microspheres, and 10 mM n-octadecyltrimethoxysilane was added to the ethanol. The mixture was left on a shaker for 12 hours, then centrifuged and the supernatant disposed of. The microspheres were rinsed one last time in ethanol then dispersed in the oil-surfactant mixture, by vortex mixing for a few seconds, followed by sonication for 5 minutes, to avoid clumping of the microspheres. The particles in Figure 3.10 were prepared according to this protocol.

3.4.7 Image acquisition and analysis

The Andor iXon camera was used to acquire videos of droplets and particles flowing through the device. Acquisition parameters were adjusted for different operating conditions, but in general, the frame rate was on the order of 10 frames/s, exposure time on the order of 0.1-1 ms, and each video captured spanned around 30 s.

In order to extract the streak lengths, hence velocities, from the images, we wrote a MATLAB code to perform this task in a semi-automatic manner. A screen capture of the running program is shown in Figure 3.11. The user needs to click on the streaks they wish to identify, and the code determines their lengths, the channels they're in, and calculates and displays the velocity distribution in each channel.

Since the flow profile in the channels was three-dimensional while the acquired streak images were two-dimensional, two potential sources of error came to our attention: firstly, that an image would contain streaks from different planes, therefore by lumping them all together we would be building an incorrect image of the velocity distribution; and secondly, we were assuming that the streaks were all confined to a horizontal plane, while they could have vertical components, which would yield incorrect velocity estimates. We attempted to minimize the effect of the first source of error by focusing the image on the middle plane of the device, in

order to observe the maximum velocities in the channels, and excluding images from other planes. In order to do that, we used a 20X objective with a numerical aperture (N.A.) of 0.45, which yielded a depth-of-field *(dof)*[61]

$$dof = \frac{\lambda}{2(\text{N.A})^2} \approx 1.2\,\mu\text{m} \ .$$

Therefore, theoretically, the depth-of-field was limited to 5% of the channels depth, and by using 1-μm microspheres, the depth-of-field corresponded to one plane of microspheres. Experimentally, we would typically observe streaks with different brightness levels, and we would only consider those that had similar bightness. Finally, in the event where several streaks would be at the same location, have the same brightness level, and different lengths, we would consider the longest ones (since only the maximum velocities were desired).

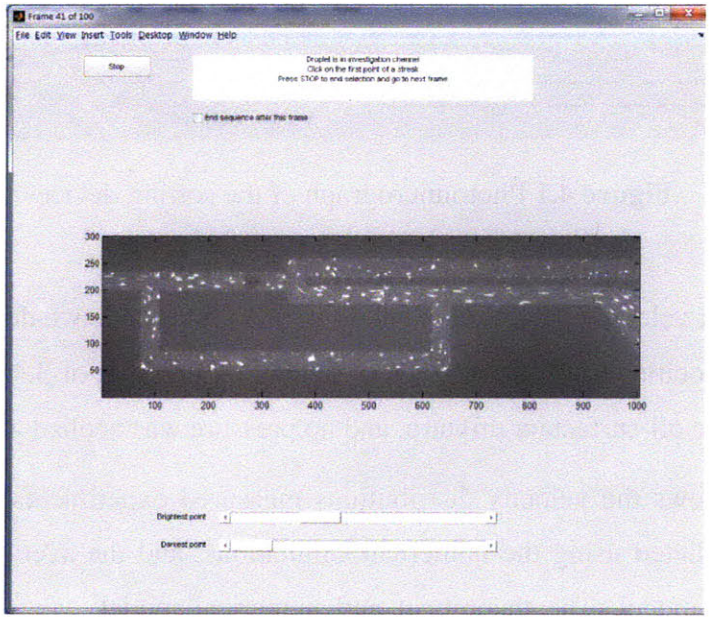

Figure 3.11 MATLAB screen capture

Chapter 4

Results and Discussion

4.1 Device Characterization

Figure 4.1 shows an image of the circuit used in the sorting experiments of droplets, based on the calculations of Chapter 3.

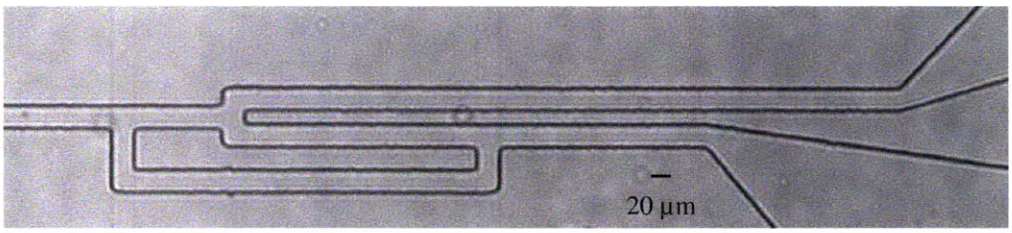

Figure 4.1 Photomicrograph of the sorting device

Particle streak velocimetry technique and the MATLAB code we developed were used to measure the flow velocities in the unobstructed channel. A pressure of 3.45 kPa was applied on the vial containing the oil-surfactant mixture, and no pressure was applied at the outlets.

Figure 4.2 shows the velocity distributions measured experimentally, together with the velocity profiles predicted using the numerical simulations, and the average velocity predicted using the resistance model. The theoretical and numerical models were modified slightly to incorporate the additional resistance resulting from the flexible tubing, which yielded a pressure of 3 kPa being applied at the entrance of the input channel.

We note that the velocity distributions obtained experimentally match the expected device performance: the average flow velocity in the sensing channel is more than double that in the bypass channel, and the velocity in the lower output channel is higher than that in the upper output channel. However, we note that the experimental and theoretical results are off by a factor

of 1.5-2. We believe this discrepancy could be attributed to physical factors, such as leakage from the pressure supply system, resulting in a lower effective pressure being applied to the oil; inaccuracies in the microfabrication of the devices, or the viscosity of the oil used being higher than the reported value.

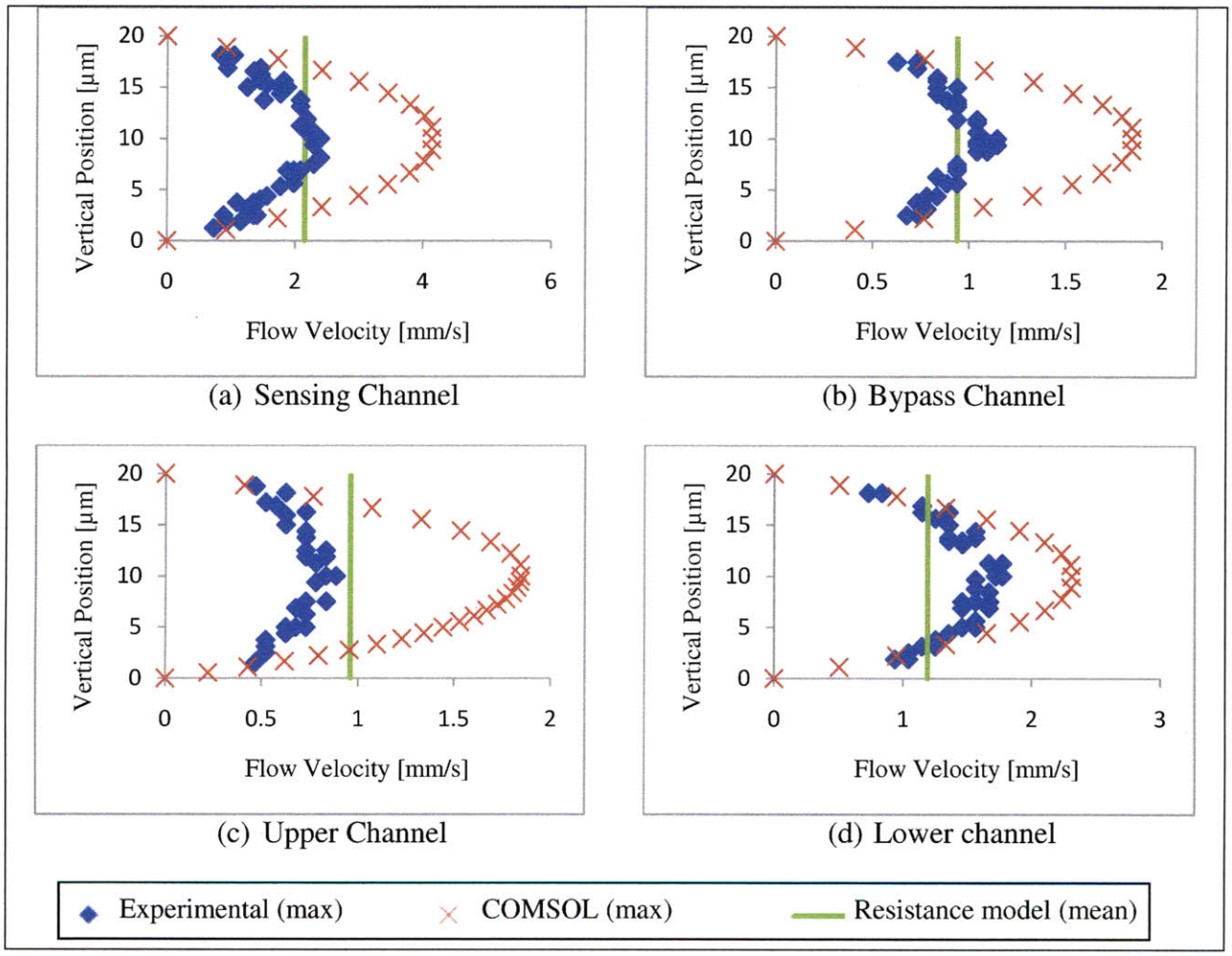

Figure 4.2 Measured and predicted flow velocities

4.2 Sorting of Gelatin Particles

4.2.1 Particle characterization

We used the differential manometer to measure the additional hydrodynamic resistance induced by a gelatin particle traveling in the sensing channel. Figure 4.3 shows the relationship between the particle size and the additional hydrodynamic resistance it induces (R_p), expressed as a fraction of the resistance of the unobstructed channel (R_c). The particle size is expressed as a fraction of the hydraulic diameter of the channel, which in turn is given by

$$D_h = \frac{4 \cdot Area}{Perimeter} \tag{4.1}$$

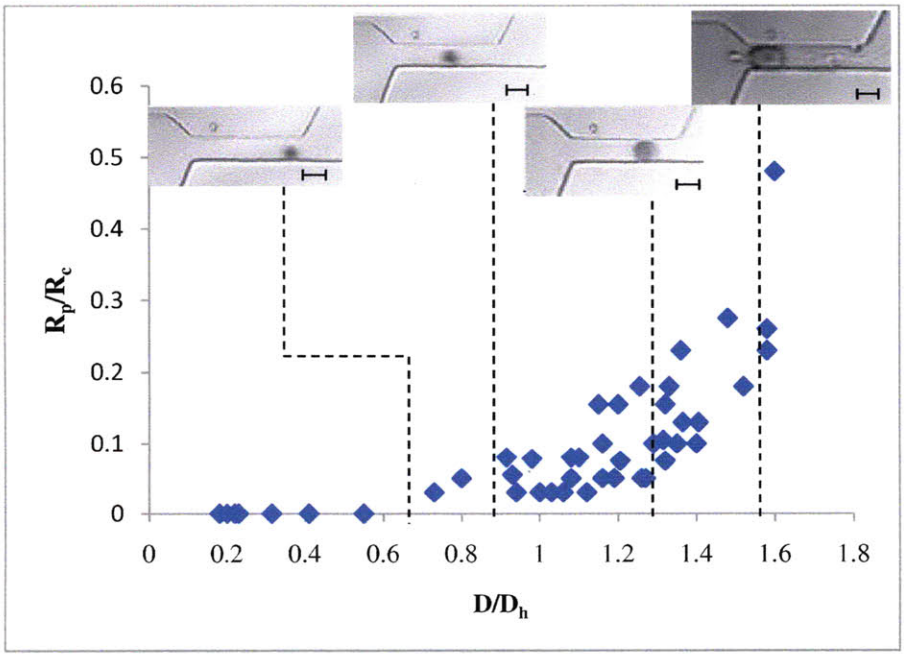

Figure 4.3 Hydrodynamic resistance of gelatin particles vs. particle size. Horizontal axis is the particle diameter as a fraction of the hydraulic diameter of the channel; vertical axis is the hydrodynamic resistance induced by the particle, expressed as a fraction of the resistance of the unobstructed channel (R_p/R_c). Insets show particles of different sizes in the channel. Scale bars are 20 μm. Figure courtesy of Mr. Marco Cartas.

We find that particles with diameters less than 75% of the hydraulic diameter of the channel did not induce any measureable resistance. As the particle size increased, the additional resistance increased exponentially, reaching a maximum of about 25% of that of the unobstructed channel, when the particle diameter was approximately 1.5 times that of the channel.

4.2.2 Gelatin sorting experiments

A suspension of gelatin particles was prepared according to the protocol outlined in Chapter 3 and introduced through the input channel under a pressure of 8 psi, while the pressures at the outlets were kept at zero. Videos were captured of the particles traveling through the device and being sorted at the two outlets. We were not able, however, to reliably measure the changes in velocity resulting from the presence of a particle in the sensing channel: the transit time of a particle through the sensing channel was approximately equal to the time between two successive frames; this usually resulted in only one frame where the particle was in the sensing channel, which did not allow for sufficient data points to measure the velocities in that case.

We measured the particle size distribution at each outlet by examining the apparent diameter of the particles in the exit reservoirs connected to the output channels. Figure 4.4 shows the particle size distribution at the 2 outlets. We notice that particles less than 12.2 μm (zone I) were almost evenly distributed among the 2 outlets, without any observed sorting effect. For the larger particles, we find that 22 out of the 23 particles ranging in size between 12.2 μm and 17.8 μm (zone II) exited from the lower channel, while all particles larger than 17.8 μm (17 particles of diameters between 17.8 μm and 28.9 μm, zone III) exited through the upper channel. This behavior was repeatabl e, and could be explained as follows:

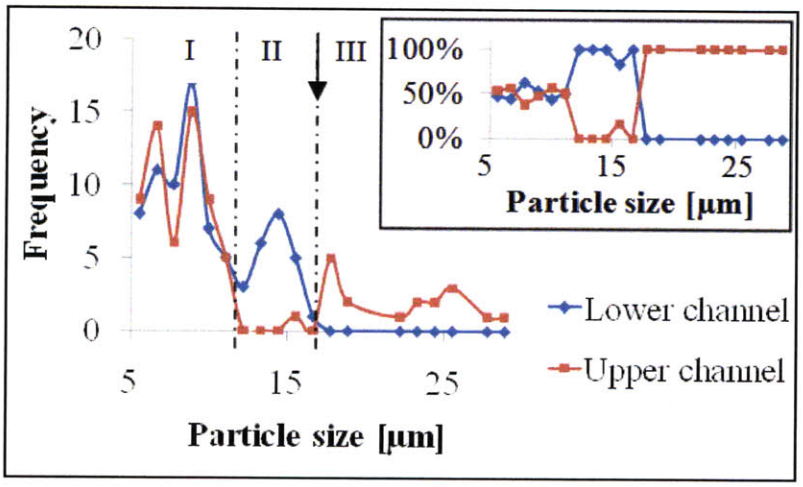

Figure 4.4 Particle size distribution at the outlets for P_{in}=8psi, P_1=P_2=0. The arrow points to the cutoff particle size. Inset: fraction of each particle size at the outlets.

The small particles (<12.2 μm) do not exhibit any sorting behavior due to their small size compared to the channel which allows them to follow the streamlines into either outlet channel. Particles in the intermediate size range (12.2 μm – 17.8 μm), however, are centered in the sensing channel, but the induced resistance is not sufficient to reverse the junction bias. Therefore, as they reach the sorting junction, they follow the lower channel which has the highest instantaneous flow rate. Finally, the largest particles (> 17.8 μm) induce a resistance high enough to bias the flow towards the upper output channel and follow that route.

From this we conclude that once the particles have a size comparable to that of the channel (in this case, $\frac{D}{D_h} > 0.6$), sorting based on size is possible. The cutoff size was approximately 18 μm $\left(\frac{D}{D_h} \approx 0.9\right)$, and the sorted particles (above 17.8 μm) had a 100% recovery rate and 94% purity (not counting the particles in zone I).

Comparing this result to the theoretical predictions of the device performance (Figure 2.8) and the results obtained from the manometer experiments (Figure 4.3), we note the following: from Figure 2.8, we would expect the bias switch to occur when R_S/R_c = 1.4; however, from Figure 4.3 we see that when D/D_h = 0.9, $R_S/R_c \approx 1.1$, and yet, the switching has

occurred. We believe this difference could very well be attributed to either the limitations of the resistance model in fully predicting the flow rates (as has been also suggested by the error between the results obtained using the model and those obtained numerically), or to inaccuracies in fabrication, which would alter both the flow rates and the relative resistances from the predicted values.

4.2.3 Effect of output pressure

Next, we increased the pressure at the upper output channel to 3 psi; we expect this to increase the threshold switching resistance, hence size cutoff, since a larger resistance would be required to bias the flow towards the upper channel. Indeed, we found that the threshold particle size increased from around 17.8 μm to around 22 μm: particles of 23.3 μm or larger exited through the upper channel, while particles ranging in size between 13.3 μm and 21.1 μm exited through the lower channel, and those smaller than 10 μm exited at either outlet. The size distribution of the particles at the outlets for this case is shown in Figure 4.5.

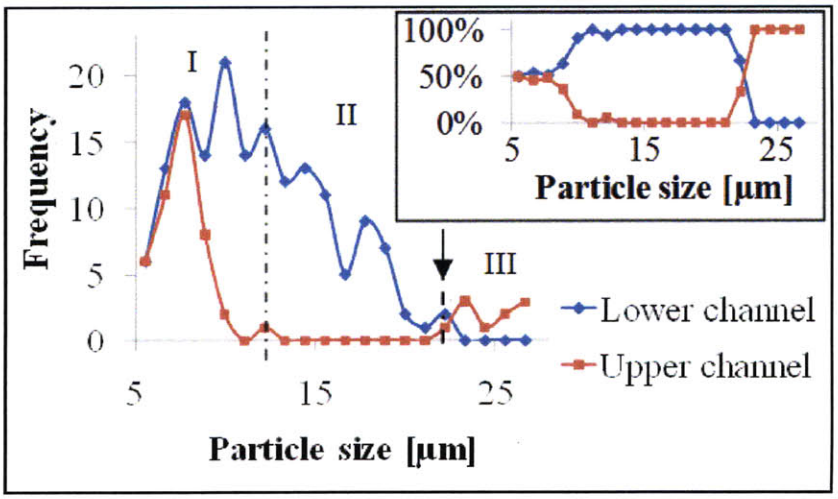

Figure 4.5 Particle size distribution at the outlets for P_{in}=8 psi, P_1=3 psi, P_2=0

4.2.4 Effect of input pressure

We reduced the supply pressure to 5 psi and repeated the experiment to investigate whether the conditions under which the particles are delivered would have an effect on the

sorting outcome. The sorting results are shown in Figure 4.6 when the output pressures are set to zero. We note that the cutoff size has increased to approximately 23 μm. Figure 4.7 shows the sorting results under the same supply pressure but with the output pressure raised to 2 psi. The cutoff size was found to be approximately 27.5 μm.

We believe the increase in the cutoff size could be due to the relaxation of the flow back to its unperturbed state as soon as the particle exits the sensing channel and before it enters an output channel. The slower flow rate enables the flow to relax faster as compared to the transit time of the particle; hence, a larger particle is needed to effect the switching.

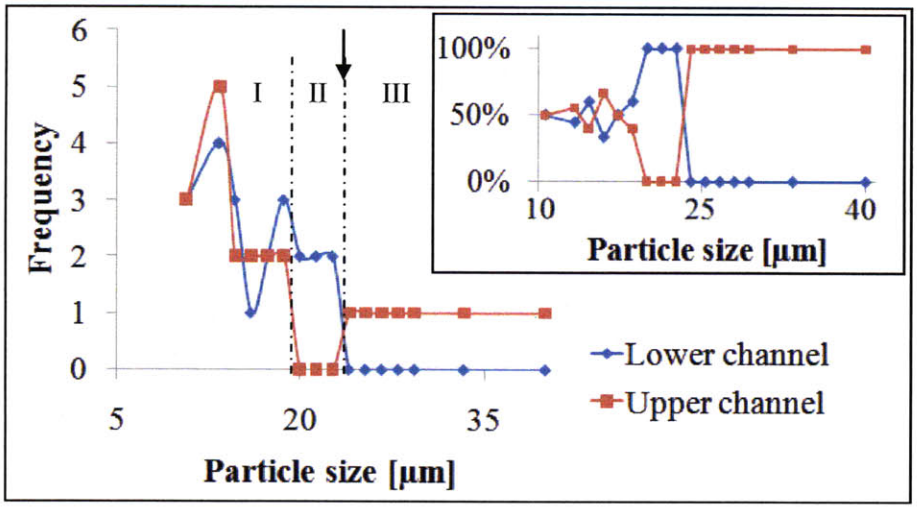

Figure 4.6 Particle size distribution at the outlets for P_{in}=5 psi, P_1=3 psi, P_2=0

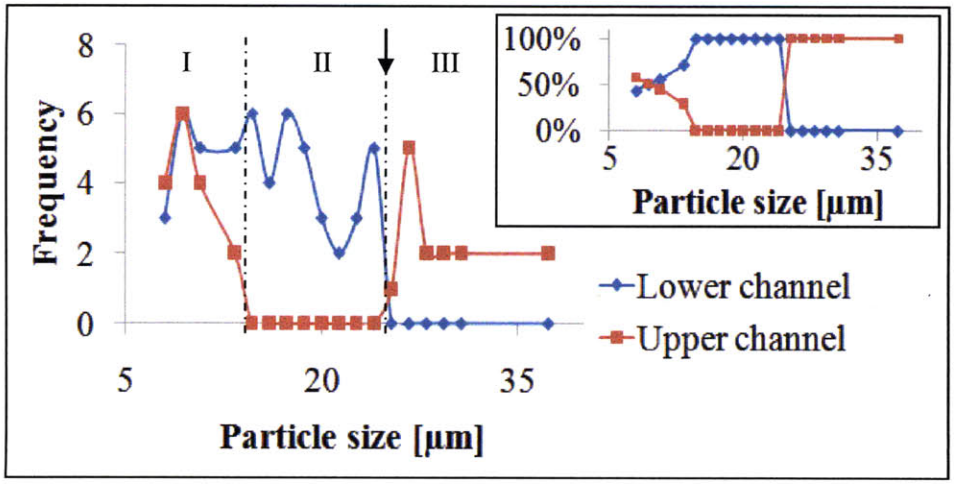

Figure 4.7 Particle size distribution at the outlets for P_{in}=5 psi, P_1=2 psi, P_2=0

4.3 Sorting of Droplets

To demonstrate sorting based on deformability, we conducted sorting experiments on two types of droplets: water droplets and glycerol droplets, both dispersed in oil. Glycerol has a viscosity of 1 $N \cdot s/m^2$, rendering it one thousand times more viscous than water. Therefore, a glycerol droplet is expected to be less deformable and to exhibit a much higher resistance to flow than a water droplet.

Using a sorting circuit with two T-junctions upstream to generate the droplets, we found that the water droplets exited the device through the lower channel, while the glycerol droplets exited through the upper channel. This result is shown in Figure 4.8, and suggests that the device is able to detect changes in droplet viscosity, as gets translated into a change in hydrodynamic resistance. However, we note that the droplets had a slightly different size: the water droplet had an average size of 33 μm while the glycerol droplets had an average size of 35 μm. This was due to the fact that flow rates could not be set with sufficient accuracy so as to yield equal-sized droplets. Therefore, more investigation is necessary in order to ensure that the sorting was indeed due to the difference in viscosity or deformability.

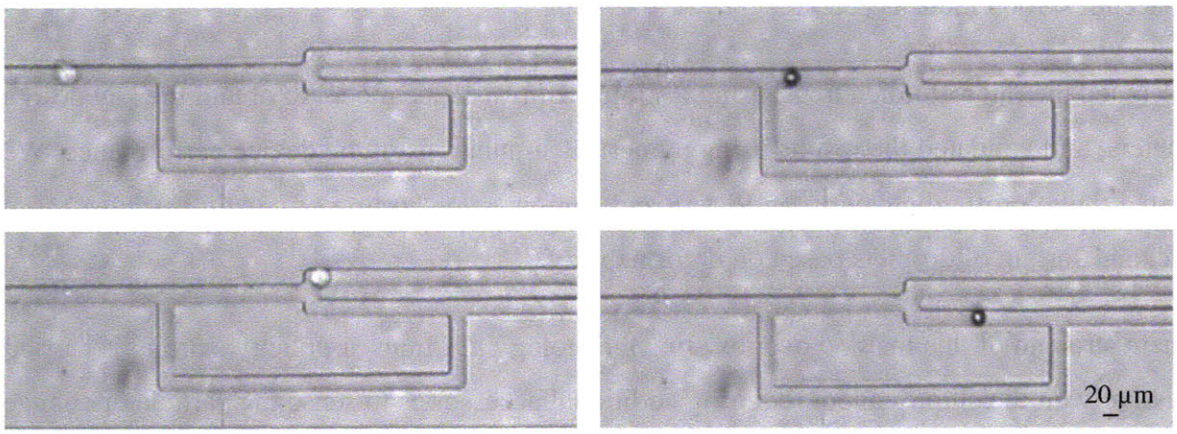

Figure 4.8 Sorting of droplets. Glycerol droplets (light) to the top channel and water droplets (dark) to the bottom channel.

Chapter 5

Conclusions and Future Work

Sorting of cells and droplets is a critical tool in in medicine, research, and industry. Among the different techniques available to sort cells and droplets, sorting based on physical properties, such as size and deformability, stands out as a relatively simple technique with a wide range of applications.

In this work, we presented a new method to sort deformable particles based on the hydrodynamic resistance they induce in microchannels. The sorting criterion – hydrodynamic resistance – could be related to different physical properties, such as size, deformability, shape, etc. This could find application in cell sorting and bioseparation for research, therapeutics, and point-of-care diagnostics, as well as in the industrial applications of two-phase microfluidics, e.g., pharmaceutics, food industry, etc.

We designed the microfluidic circuit using a simplified resistance model to obtain the key design parameters, and validated the results using numerical simulations of the device performance. We fabricated the microfluidic devices in PDMS and demonstrated sorting of gelatin particles based on size, and sorting of droplets based on deformability.

The main strength of this method over existing technology lies in its simplicity: sorting is carried out passively on the chip, without requiring additional accessories to sense the particle or change its path. Moreover, the device can be easily customized to change the sorting parameter or the sorting threshold without requiring new design or fabrication, and multiple devices can be combined in parallel (to increase throughput) or in series (to increase resolution).

The device's ease of operation, combined with the low cost of its components, make it a good candidate for portability, e.g., for point-of-care applications, or rural areas with limited access to such facilities.

5.1 Future Work

In our experiments, sorting was demonstrated on particles having different size or deformability while the other parameter was kept constant. However, it would be very beneficial to explore the possibility of targeting one parameter as the sorting criterion regardless of variations in other parameters.

Towards this end, better characterization of the device performance is necessary. We were limited by the capabilities of our camera, however, a high speed camera and either particle image velocimetry (PIV) or particle streak velocimetry (PSV) are needed to detect the changes in velocities induced by particles in the sensing channel, which would yield a better understanding of how the device works, and its different modes of operation.

Finally, the ultimate test for this method would be in its application in cell sorting. Possible applications include separation and enrichment of circulating tumor cells from blood, sorting of stem cells, and the separation of malaria-infected red blood cells from healthy red blood cells.

References

1. Lee, G.Y.H. and Lim, C.T., *Biomechanics approaches to studying human diseases.* Trends in Biotechnology, 2007. **25**(3): p. 111-118.
2. Vaziri, A. and Gopinath, A., *Cell and biomolecular mechanics in silico.* Nature Materials, 2007. **7**(1): p. 15-23.
3. Diez-Silva, M., Dao, M., Han, J.Y., Lim, C.-T., and Suresh, S., *Shape and biomechanical characteristics of human red blood cells in health and disease.* MRS BULLETIN. **35**: p. 382-388.
4. Suresh, S., *Biomechanics and biophysics of cancer cells.* Acta Materialia, 2007. **55**(12): p. 3989-4014.
5. Cranston, H.A., Boylan, C.W., Carroll, G.L., Sutera, S.P., Williamson, J.R., Gluzman, I.Y., and Krogstad, D.J., *Plasmodium falciparum maturation abolishes physiologic red cell deformability.* Science, 1984. **223**(4634): p. 400.
6. Dondorp, A.M., Pongponratn, E., and White, N.J., *Reduced microcirculatory flow in severe falciparum malaria: pathophysiology and electron-microscopic pathology.* Acta tropica, 2004. **89**(3): p. 309-317.
7. Ballas, S.K., *Sickle cell anemia with few painful crises is characterized by decreased red cell deformability and increased number of dense cells.* American journal of hematology, 1991. **36**(2): p. 122-130.
8. Baerlocher, G.M., Meiselmanb, H.J., and Reinhart, W.H., *Gel-filtration of sickle erythrocytes: separation based on cell deformability.* Clinical hemorheology and microcirculation, 2001. **24**(1): p. 11-18.
9. Moutzouri, A.G., Skoutelis, A.T., Gogos, C.A., Missirlis, Y.F., and Athanassiou, G.M., *Red blood cell deformability in patients with sepsis: a marker for prognosis and monitoring of severity.* Clinical hemorheology and microcirculation, 2007. **36**(4): p. 291-299.
10. Drost, E.M., Kassabian, G., Meiselman, H.J., Gelmont, D., and Fisher, T.C., *Increased rigidity and priming of polymorphonuclear leukocytes in sepsis.* American journal of respiratory and critical care medicine, 1999. **159**(6): p. 1696.
11. Vona, G., Sabile, A., Louha, M., Sitruk, V., Romana, S., Schutze, K., Capron, F., Franco, D., Pazzagli, M., and Vekemans, M., *Isolation by Size of Epithelial Tumor Cells: A New Method for the Immunomorphological and MolecularCharacterization of Circulating Tumor Cells.* American Journal of Pathology, 2000. **156**(1): p. 57.
12. Suresh, S., Spatz, J., Mills, J.P., Micoulet, A., Dao, M., Lim, C.T., Beil, M., and Seufferlein, T., *Connections between single-cell biomechanics and human disease states: gastrointestinal cancer and malaria.* Acta Biomaterialia, 2005. **1**(1): p. 15-30.
13. Guck, J., Schinkinger, S., Lincoln, B., Wottawah, F., Ebert, S., Romeyke, M., Lenz, D., Erickson, H.M., Ananthakrishnan, R., and Mitchell, D., *Optical Deformability as an Inherent Cell Marker for Testing Malignant Transformation and Metastatic Competence.* Biophysical Journal, 2005. **88**(5): p. 3689-3698.
14. Sia, S.K. and Whitesides, G.M., *Microfluidic devices fabricated in poly (dimethylsiloxane) for biological studies.* Electrophoresis, 2003. **24**(21): p. 3563-3576.

15. Song, H., Chen, D.L., and Ismagilov, R.F., *Reactions in droplets in microfluidic channels.* Angewandte chemie international edition, 2006. **45**(44): p. 7336-7356.
16. Teh, S.Y., Lin, R., Hung, L.H., and Lee, A.P., *Droplet microfluidics.* Lab on a Chip, 2008. **8**(2): p. 198-220.
17. Link, D.R., Grasland-Mongrain, E., Duri, A., Sarrazin, F., Cheng, Z., Cristobal, G., Marquez, M., and Weitz, D.A., *Electric Control of Droplets in Microfluidic Devices.* Angewandte Chemie, 2006. **118**(16): p. 2618-2622.
18. Tan, Y.C. and Lee, A.P., *Microfluidic separation of satellite droplets as the basis of a monodispersed micron and submicron emulsification system.* Lab on a Chip, 2005. **5**(10): p. 1178-1183.
19. Heusch, R. and Leverkusen, B.A.G., *Ullmann's Encyclopedia of Industrial Chemistry, 2000.* DOI. **10**: p. 14356007.
20. Lai, C.-W., Lin, Y.-H., and Lee, G.-B., *A microfluidic chip for formation and collection of emulsion droplets utilizing active pneumatic micro-choppers and micro-switches.* Biomedical Microdevices, 2008. **10**(5): p. 749-756.
21. Bhagat, A.A.S., Bow, H., Hou, H.W., Tan, S.J., Han, J., and Lim, C.T., *Microfluidics for cell separation.* Medical and Biological Engineering and Computing, 2010: p. 1-16.
22. Schmid-Schönbein, H., Weiss, J., and Ludwig, H., *A simple method for measuring red cell deformability in models of the microcirculation.* Annals of Hematology, 1973. **26**(6): p. 369-379.
23. Reid, H.L., Barnes, A.J., Lock, P.J., Dormandy, J.A., and Dormandy, T.L., *A simple method for measuring erythrocyte deformability.* British Medical Journal, 1976. **29**(9): p. 855.
24. Bessis, M. and Mohandas, N., *A diffractometric method for the measurement of cellular deformability.* Blood Cells, 1975. **1**(3): p. 307-313.
25. Stuart, J., Stone, P.C.W., Bareford, D., Caldwell, N.M., Davies, J.E., and Baar, S., *EVALUATION OF LEUKOCYTE REMOVAL METHODS FOR STUDIES OF ERYTHROCYTE DEFORMABILITY.* Clinical hemorheology, 1985. **5**(2): p. 137-147.
26. Baskurt, Oguz K., Gelmont, D., and Meiselman, Herbert J., *Red Blood Cell Deformability in Sepsis.* Am. J. Respir. Crit. Care Med., 1998. **157**(2): p. 421-427.
27. Rosenbluth, M.J., Lam, W.A., and Fletcher, D.A., *Analyzing cell mechanics in hematologic diseases with microfluidic biophysical flow cytometry.* Lab on a Chip, 2008. **8**(7): p. 1062-1070.
28. Hochmuth, R.M., *Micropipette aspiration of living cells.* Journal of Biomechanics, 2000. **33**(1): p. 15-22.
29. Paulitschke, M. and Nash, G.B., *Micropipette methods for analysing blood cell rheology and their application to clinical research.* Clinical hemorheology, 1993. **13**(4): p. 407-434.
30. Tracey, M.C., Greenaway, F.S., Das, A., Kaye, P.H., and Barnes, A.J., *A silicon micromachined device for use in blood cell deformability studies.* Biomedical Engineering, IEEE Transactions on, 1995. **42**(8): p. 751-761.
31. Whitesides, G.M., *The origins and the future of microfluidics.* Nature, 2006. **442**(7101): p. 368-373.
32. Huang, L.R., Cox, E.C., Austin, R.H., and Sturm, J.C., *Continuous Particle Separation Through Deterministic Lateral Displacement.* Science, 2004. **304**(5673): p. 987-990.

33. Mohamed, H., Murray, M., Turner, J.N., and Caggana, M., *Isolation of tumor cells using size and deformation.* Journal of Chromatography A, 2009. **1216**(47): p. 8289-8295.
34. Wilding, P., Kricka, L.J., Cheng, J., Hvichia, G., Shoffner, M.A., and Fortina, P., *Integrated Cell Isolation and Polymerase Chain Reaction Analysis Using Silicon Microfilter Chambers* 1.* Analytical biochemistry, 1998. **257**(2): p. 95-100.
35. Di Carlo, D., Irimia, D., Tompkins, R.G., and Toner, M., *Continuous inertial focusing, ordering, and separation of particles in microchannels.* Proceedings of the National Academy of Sciences, 2007. **104**(48): p. 18892.
36. Di Carlo, D., *Inertial microfluidics.* Lab on a Chip, 2009. **9**(21): p. 3038.
37. Yamada, M., Nakashima, M., and Seki, M., *Pinched Flow Fractionation: Continuous Size Separation of Particles Utilizing a Laminar Flow Profile in a Pinched Microchannel.* ANALYTICAL CHEMISTRY-WASHINGTON DC-, 2004. **76**: p. 5465-5471.
38. Tan, Y.C., Fisher, J.S., Lee, A.I., Cristini, V., and Lee, A.P., *Design of microfluidic channel geometries for the control of droplet volume, chemical concentration, and sorting.* Lab on a Chip, 2004. **4**(4): p. 292-298.
39. Yamada, M. and Seki, M., *Hydrodynamic filtration for on-chip particle concentration and classification utilizing microfluidics.* Lab on a Chip, 2005. **5**(11): p. 1233-1239.
40. Yamada, M., Kano, K., Tsuda, Y., Kobayashi, J., Yamato, M., Seki, M., and Okano, T., *Microfluidic devices for size-dependent separation of liver cells.* Biomedical Microdevices, 2007. **9**(5): p. 637-645.
41. Agresti, J.J., Antipov, E., Abate, A.R., Ahn, K., Rowat, A.C., Baret, J.C., Marquez, M., Klibanov, A.M., Griffiths, A.D., and Weitz, D.A., *Ultrahigh-throughput screening in drop-based microfluidics for directed evolution.* Proceedings of the National Academy of Sciences, 2010. **107**(9): p. 4004.
42. Hu, X., Bessette, P.H., Qian, J., Meinhart, C.D., Daugherty, P.S., and Soh, H.T., *Marker-specific sorting of rare cells using dielectrophoresis.* Proceedings of the National Academy of Sciences, 2005. **102**(44): p. 15757.
43. Akagi, T. and Ichiki, T., *Cell electrophoresis on a chip: what can we know from the changes in electrophoretic mobility?* Analytical and bioanalytical chemistry, 2008. **391**(7): p. 2433-2441.
44. Wang, M.M., Tu, E., Raymond, D.E., Yang, J.M., Zhang, H., Hagen, N., Dees, B., Mercer, E.M., Forster, A.H., Kariv, I., Marchand, P.J., and Butler, W.F., *Microfluidic sorting of mammalian cells by optical force switching.* Nat Biotech, 2005. **23**(1): p. 83-87.
45. Ozkan, M., Wang, M., Ozkan, C., Flynn, R., and Esener, S., *Optical manipulation of objects and biological cells in microfluidic devices.* Biomedical Microdevices, 2003. **5**(1): p. 61-67.
46. Vanapalli S. A., G., D.M.H., and Mugele F, *Microfluidics as a functional tool for cell mechanics.* Biomicrofluidics, 2009. **3**(1): p. 012006.
47. Engl, W., Roche, M., Colin, A., Panizza, P., and Ajdari, A., *Droplet Traffic at a Simple Junction at Low Capillary Numbers.* Physical Review Letters, 2005. **95**(20): p. 208304.
48. Link, D.R., Anna, S.L., Weitz, D.A., and Stone, H.A., *Geometrically Mediated Breakup of Drops in Microfluidic Devices.* Physical Review Letters, 2004. **92**(5): p. 054503.
49. Briscoe, B.J., Lawrence, C.J., and Mietus, W.G.P., *A review of immiscible fluid mixing.* Advances in Colloid and Interface Science, 1999. **81**(1): p. 1-17.

50. Fuerstman, M.J., Garstecki, P., and Whitesides, G.M., *Coding/Decoding and Reversibility of Droplet Trains in Microfluidic Networks.* Science, 2007. **315**(5813): p. 828.
51. Prakash, M. and Gershenfeld, N., *Microfluidic Bubble Logic.* Science, 2007. **315**(5813): p. 832.
52. Bruus, H., *Theoretical microfluidics.* 2008: Oxford University Press, USA.
53. Squires, T.M. and Quake, S.R., *Microfluidics: Fluid physics at the nanoliter scale.* Reviews of Modern Physics, 2005. **77**(3): p. 977.
54. McDonald, J.C., Duffy, D.C., Anderson, J.R., Chiu, D.T., Wu, H., Schueller, O.J.A., and Whitesides, G.M., *Fabrication of microfluidic systems in poly (dimethylsiloxane).* Electrophoresis, 2000. **21**(1): p. 27-40.
55. Ng, J.M.K., Gitlin, I., Stroock, A.D., and Whitesides, G.M., *Components for integrated poly(dimethylsiloxane) microfluidic systems.* Electrophoresis, 2002. **23**(20): p. 3461-3473.
56. Stoklosa, M.J. and Ansel, H.C., *Pharmaceutical calculations.* 1974: Lea & Febiger.
57. Opawale, F.O. and Burgess, D.J., *Influence of Interfacial Properties of Lipophilic Surfactants on Water-in-Oil Emulsion Stability* 1.* Journal of colloid and interface science, 1998. **197**(1): p. 142-150.
58. Abkarian, M., Faivre, M., and Stone, H.A., *High-speed microfluidic differential manometer for cellular-scale hydrodynamics.* Proceedings of the National Academy of Sciences, 2006. **103**(3): p. 538-542.
59. Thorsen, T., Roberts, R.W., Arnold, F.H., and Quake, S.R., *Dynamic Pattern Formation in a Vesicle-Generating Microfluidic Device.* Physical Review Letters, 2001. **86**(18): p. 4163-4166.
60. Dimotakis, P.E., Debussy, F.D., and Koochesfahani, M.M., *Particle streak velocity field measurements in a two dimensional mixing layer.* Physics of Fluids, 1981. **24**: p. 995.
61. Hecht, E., *Optics.* 2001, Addison Wesley.